



An inverse modeling approach for semilunar heart valve leaflet mechanics: exploitation of tissue structure

Ankush Aggarwal¹ · Michael S. Sacks¹

Received: 9 April 2015 / Accepted: 23 September 2015 / Published online: 8 October 2015
© Springer-Verlag Berlin Heidelberg 2015

Abstract Determining the biomechanical behavior of heart valve leaflet tissues in a noninvasive manner remains an important clinical goal. While advances in 3D imaging modalities have made *in vivo* valve geometric data available, optimal methods to exploit such information in order to obtain functional information remain to be established. Herein we present and evaluate a novel leaflet shape-based framework to estimate the biomechanical behavior of heart valves from surface deformations by exploiting tissue structure. We determined accuracy levels using an “ideal” *in vitro* dataset, in which the leaflet geometry, strains, mechanical behavior, and fibrous structure were known to a high level of precision. By utilizing a simplified structural model for the leaflet mechanical behavior, we were able to limit the number of parameters to be determined per leaflet to only two. This approach allowed us to dramatically reduce the computational time and *easily* visualize the cost function to guide the minimization process. We determined that the image resolution and the number of available imaging frames were important components in the accuracy of our framework. Furthermore, our results suggest that it is possible to detect differences in fiber structure using our framework, thus allowing an opportunity to diagnose asymptomatic valve diseases and begin treatment at their early stages. Lastly, we observed good agreement of the final resulting stress–strain response when an averaged fiber architecture was used. This suggests that population-averaged fiber structural data may

be sufficient for the application of the present framework to *in vivo* studies, although clearly much work remains to extend the present approach to *in vivo* problems.

Keywords Heart valves · Inverse model · Semilunar leaflets · Tissue microstructure

Nomenclature and symbol definitions

Γ	Fiber orientation distribution function
θ, θ_0	Fiber direction and the preferred fiber direction respectively
OI	Fiber splay in terms of orientation index
σ	Fiber splay in terms of standard deviation of orientation distribution function
$\Psi, \Psi_f, \Psi_m, \Psi^{\text{ens}}$	Elastic strain energy (total, fiber contribution, matrix contribution and ensemble respectively)
$\bar{\lambda}, \mu$	Lamé constants in compressible neo-Hookean model
\bar{E}, ν	Young’s modulus and Poisson’s ratio
\mathbf{N}	Fiber direction vector in reference configuration
\mathbf{E}, \mathbf{C}	Strain (Green–Lagrange and right Cauchy–Green tensors respectively)
I_1, J	First and third invariants of right Cauchy–Green strain tensor
d_e	Anisotropy parameter
E_{ens}	Ensemble strain
c_0, c_1	Material parameters in the fiber part

✉ Michael S. Sacks
msacks@ices.utexas.edu

¹ Center for Cardiovascular Simulation, Institute for Computational Engineering and Sciences, Department of Biomedical Engineering, The University of Texas at Austin, 201 East 24th Street, POB 5.438, 1 University Station, C0200, Austin, TX 78712-0027, USA

$w_{\theta i}$	Weights in the Gauss quadrature rule
χ	Lagrange multiplier in contact constraint
μ_f	Coefficient of friction between leaflets
$\Delta t_{\min}, \Delta t_{\max}$	Time step (minimum and maximum)
\mathbf{U}	Displacement vector
E	Total energy of the system
$\mathbf{x}_i^\alpha, \tilde{\mathbf{x}}_i^\alpha$	Coordinates of point cloud and its projection on the deformed mesh
$\mathcal{F}, \mathcal{F}_{\min}, \mathbf{J}$	Objective function, its value at the absolute minima and corresponding gradient vector
λ	Damping-like parameter in Levenberg-Marquardt algorithm
$\Theta_j(\mathbf{v}_{1j}, \mathbf{v}_{2j}, \mathbf{v}_{3j}, \mathbf{v}_{4j})$	Linear quadrilateral element defined by its four vertices
\bar{c}_0, \bar{c}_1	Known material parameters in the fiber part

1 Introduction

Heart valves control blood flow during each cardiac cycle, and any deviation from the optimal closing-opening behavior affecting basic indices, such as lower cardiac output, often contributes to heart failure. Different types of valve diseases can cause such abnormal behavior, including, but not limited to, aortic stenosis, regurgitation, and calcific disease (Rajamannan 2013). These diseases all have complex etiological pathways but share an intricate relationship to the mechanical properties of the valve leaflets. For example, calcific disease and stenosis lead to stiffening of the valve leaflets, making them incapable of opening fully. Mechanical stresses also contribute to the development of these pathologies by affecting the valvular interstitial cell (VIC) phenotype (Poggio et al. 2013; Yip and Simmons 2011), clearly indicating the importance of mechanical properties in valvular function. In addition, congenital anomalies which put the patient at a higher risk of developing valve disease, like bicuspid aortic valve (BAV), are observed to bear different structural characteristics and may produce an abnormal mechanical environment (Aggarwal et al. 2014). Leaflet structural and mechanical properties are known to vary among patients, with stiffening in native tissues observed with age (Christie and Barratt-Boyes 1995; Stephens et al. 2010). This suggests a strong need for patient-specific analysis, yet there is a lack of comprehensive knowledge about the valve-related disease development and progression and their relation to the ongoing changes of the mechanical properties of the leaflets. As a result, an ongoing challenge is the diagnosis of asymptomatic

patients for stratification based upon their risk of developing diseases. Moreover, prosthetic valve technology continues to be limited in terms of durability. There is thus an ongoing need to determine *in vivo* heart valve function for *in vivo* assessment of diseased and replacement valves, as well as in the development of novel replacement/repair technologies.

The most commonly used technique for determining the mechanical properties of heart valve leaflets is direct *ex vivo* experimentation (Billiar and Sacks 2000a, b; Gloeckner et al. 1999; Sacks 1999, 2000c). However, such techniques require the tissue to be explanted, preventing their usability in a clinical setting. Also, the changes in the tissue structure and shape as it is explanted (e.g., valve's reference configuration (Amini et al. 2012)) lead to challenges in relating *ex vivo* measurements of tissue to its *in vivo* behavior. To avoid the need of excision, other techniques have been developed. Elastography uses imaging along with a stimulus and, through a correlation technique, determines the stress-strain behavior of soft tissues (Ophir et al. 1991). However, this technique in its current form is limited to small strains and slow moving tissues, both of which are not applicable to heart valve leaflets. Hyperelastic warping solves the small strain limitation of elastography by using a hyperelasticity based regularization term, but it calculates only a deformation field, not the underlying mechanical properties (Veress et al. 2005). There have been other efforts by tracking the position of physical markers applied to valve leaflets during heart cycles and then using them to enforce a boundary condition in an inverse modeling setup to predict the mechanical properties of the leaflets (Krishnamurthy 2008; Lee et al. 2014; Rausch et al. 2013). However, these approaches still need physical markers to be applied—something not entirely practical to do in patients. Einstein et al. used an inverse modeling-based approach for mechanical characterization; however, the experimental data were obtained from *ex vivo* uniaxial and inflation testing setups (Einstein et al. 2005), thus again necessitating excision of the tissue.

These gaps can be filled by developing a tool that can be applied directly to the *in vivo* imaging data in order to estimate the biomechanical properties of heart valves but avoids the need for excision and the application of additional loads or physical markers. Recent advancements in 3D ultrasound technology provide an opportunity to obtain patient-specific valve images *in vivo* (Hung et al. 2007; Pouch et al. 2015). As one can obtain the shape of the leaflet as it is loaded during the closing phase of the valve using *in vivo* imaging technology (e.g., ultrasound), in principle, it is possible to extract the biomechanical properties using a “full inverse model.” On the other hand, it is not presently possible to determine the fiber structure of valve leaflets on a per-patient basis without explanting them. We recently demonstrated that population-based average fiber structure of valve leaflets can be determined for patients with BAV and found it to be fairly consis-

tent (Aggarwal et al. 2014), suggesting that such information can be obtained at least in a population-averaged sense.

However, the feasibility of such an approach and the data requirements for it to be successful are ongoing questions. For example, how many imaging frames would be needed to obtain good estimation? What is the maximum amount of information that can be realistically extracted from such a framework? Clinically relevant imaging modalities have a limit on the resolution and, thus, carry an associated error. This is compounded by the difficulty in segmenting these images to obtain tissue shape at different time points. Also, details of the leaflet fiber architecture are unknown on a patient-specific basis, which has been shown to play an important role in the mechanical behavior of valves (Sacks 2003; Sacks et al. 2009). Therefore, the question remains—would the use of population-averaged fiber structure in the inverse model give results within acceptable accuracy? What is the best way to utilize the microstructural information—the level and direction of anisotropy, while minimizing the number of unknown parameters in the constitutive model? What other input data would be needed and what are the associated accuracy requirements? The leaflets in their native environment are pre-strained (Amini et al. 2012), and thus, their reference configuration is unknown. This pre-strain has been calculated for some cases (Amini et al. 2012; Rausch et al. 2013), but remains unknown for many other cases. The other inputs to our proposed inverse model—boundary conditions (annulus position) and load conditions (the transvalvular pressure)—need to be calculated with accuracy at exact times of image acquisition.

Our long-term goal is to address this challenge through the development of a novel inverse modeling framework to determine the leaflets mechanical properties based on imaging derived quantities, coupled to a population-based supplemental database. Instead of trying to address all of these challenges simultaneously, herein we concentrate on establishing a basic framework and feasibility of our approach using an “optimal” *in vitro* dataset. We thus aim to ascertain the best framework for determining mechanical properties of valve leaflets from imaging without the need for any material point information, as well as the maximum amount of information that can be extracted.

2 Methods

2.1 General considerations

Before we describe the approach, we note that the term inverse model is often used in different contexts, and it is thus worthwhile clarifying its meaning in the context of the present work. Specifically, “forward” finite element models provide an approach where using the input data from loading and boundary conditions, and incorporating the mechanical

properties, one predicts the deformed shape of an object or system. On the other hand, “inverse models” use boundary and loading conditions and information about the deformed shape as inputs to calculate the mechanical properties. It should be noted that the deformed shape may not be completely known at all points; rather, the deformation is usually defined at a finite number of discrete positions not generally associated with material points. For such inverse models, it is usually assumed that the form of the constitutive (stress–strain) law is judiciously chosen based upon prior knowledge about the system. Therefore, the problem is reduced to calculating the parameters in the constitutive relation. Thus, the overall idea behind developing a full inverse modeling approach for heart valves is to devise a method that can use the deformation of valve leaflets during a cardiac cycle from clinically relevant imaging modalities and calculate the stress–strain behavior of valve leaflets for pathological assessments.

There are various ways of formulating inverse problems. The first common step is to construct a cost or objective function that would be minimized to obtain the final solution. Based upon the form of cost function and problem configuration, a functional minimization method is adopted. This can be achieved by gradient-based methods, where the solution is driven along the derivative of the cost function. Clearly, for such an approach to be successful, the cost function must be convex. Otherwise, the solution could be trapped in local minima. Therefore, one must be careful in defining the objective function, as it should be appropriate for clinical imaging and should also be convex to facilitate gradient-based minimization. Similarly, choosing a suitable constitutive relation is an important aspect, such that the important aspects of valve mechanics are captured without making the problem overly complicated. This is especially true in the case of soft tissues, as their mechanics are well known to be complex: They exhibit a highly nonlinear stress–strain relationship, undergo large deformations, and exhibit complex viscoelasticity and complex axial coupling behaviors that defy simple experiments and material models (Fung 1993; Sacks 2000c). Much of this behavior is a direct result of changes in their internal structure with strain, which involves both straightening of highly crimped collagen fibers and rotation of these fibers toward the stretch axis. Thus, physiologically correct simulation of heart valves requires sophisticated constitutive models which are expected to account for these behaviors. Moreover, they should be able to predict the stress environment of cells accurately in order to address the mechano-physiological questions (Lee et al. 2015).

There are many numerical challenges as well. The forward model of valve opening and closing, in itself, represents an intrinsically nonlinear problem due to the nonlinear mechanical behavior of tissues and the contact constraint between leaflets. The leaflets are usually modeled as thin shells, which

present computational challenges because of higher derivatives needed in the kinematic description and the associated locking issues (Hughes and Liu 1981a, b). The material models of valve tissue are quite complicated, and these factors lead to a forward model with a high computational cost (Sacks et al. 2009). Alongside these challenges, we have to tackle the convergence-related computational complications that the inverse modeling problem entails. Lastly, such an approach would have to be validated against extant experimental biomechanical data.

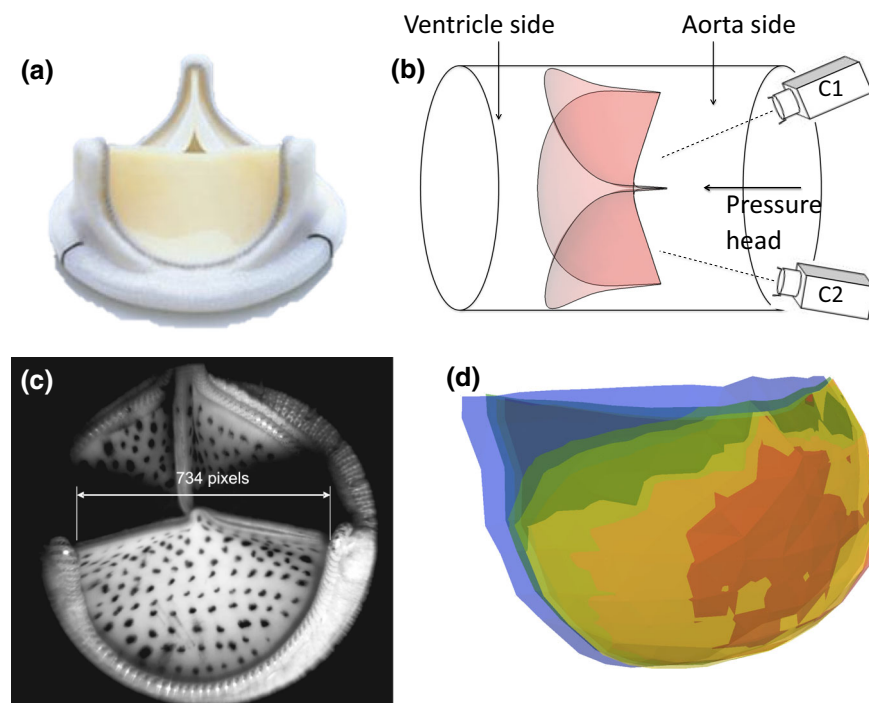
Keeping these objectives in mind, in the present study, we investigated a “best-case scenario,” in that we have all the key pieces of information: the proper reference state configuration of the valve, exact boundary and loading conditions, detailed leaflet fiber architecture, high-resolution imaging of marker spatial positions, and biaxial mechanical data for each leaflet. This allows us to formulate a high fidelity model and evaluate the effect of perturbation in each of the simulation parameters. We further concentrate on exploiting the fiber structural information and its integration into an appropriately chosen constitutive model to minimize the number of model variables. Although the present model formulation is based on in vitro data, the framework is designed from the perspective of future use of strictly in vivo image data. For example, no material point information is used since current medical imaging modalities only provide instantaneous shape and do not track material points over time. We utilize a high-resolution in vitro dataset along with detailed information about the microstructure of valve, making it possible to carry out a systematic parametric study. Most importantly, it

allowed us to determine the extent of information that can be extracted from an imaging dataset, as well as put bounds on the accuracy of the final results. Validation studies, as well as convergence and sensitivity analysis, were also conducted.

2.2 Experimental database

An experimental dataset from a previously published in vitro study was used (Sun et al. 2005), and a brief review of the experimental methods are presented. A bioprosthetic valve provided by Edwards Lifesciences Inc. (Fig. 1a, c), which is fabricated from crosslinked bovine pericardium, was put under a controlled static pressure head and imaged using two cameras (Fig. 1b). Imaging was performed using optical markers at three different pressures—40, 80 and 120 mm of Hg. In total, there were 372 markers imaged (129 on leaflet 1, 125 on leaflet 2 and 118 on leaflet 3). The fiber architecture of valve leaflets was subsequently determined using small-angle light-scattering technique (Sacks 2004; Sacks et al. 1997), from which the preferred orientation and orientation index (OI) of the fiber distribution function were calculated at each point of the leaflet (Sacks 2004; Sacks et al. 1997). Ex vivo mechanical properties of valve leaflets were then determined under biaxial loading using square sections ($\sim 10 \text{ mm} \times 10 \text{ mm}$) of leaflets following preconditioning. Thicknesses of the leaflets were measured at five points (four corners and the center) and an average was calculated for each of the three leaflets. To summarize, this dataset consisted of valve images as it was loaded, leaflets’ fiber structural information, thickness, and biaxial stress-strain data (see

Fig. 1 Experimental setup: A bovine pericardium bioprosthetic valve (a) was put under a static pressure head and imaged using two cameras from the aortic side (b), an example camera image (c) (borrowed with permission from (Sun et al. 2005)) and the triangulated point cloud of leaflet 1 image superimposed (d)—blue is at 0 mm, green is at 40 mm, yellow is at 80 mm and red is at 120 mm of Hg



summary in Table 2), with all of the following analyses being new to the present study.

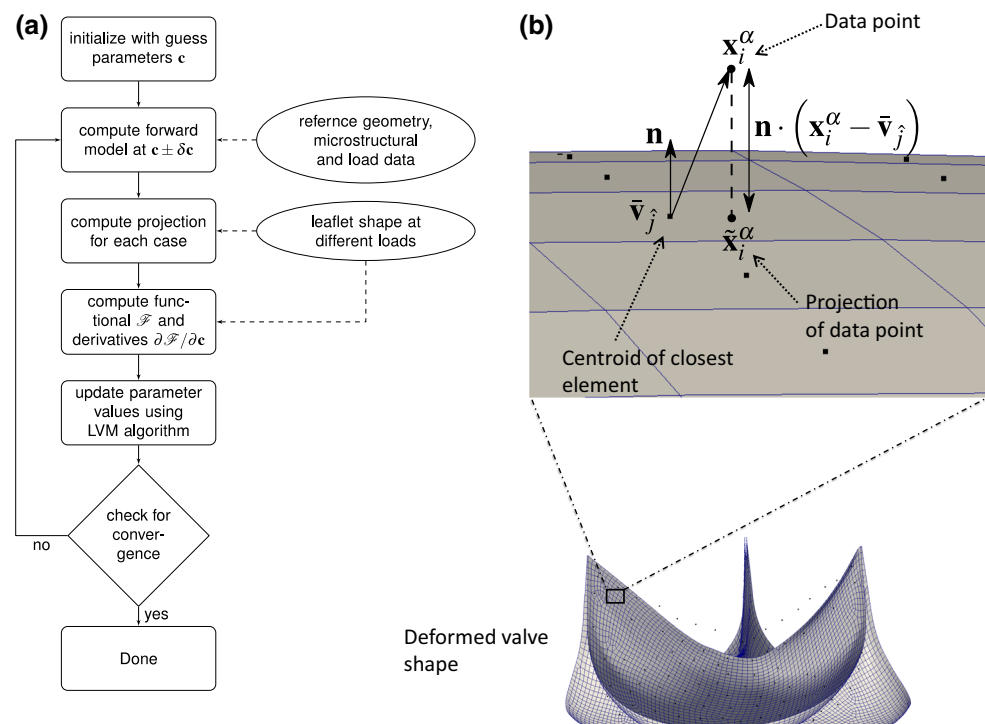
2.3 Proposed inverse modeling framework

The overall framework for our approach included starting at an initial estimate of parameter values, running a forward model and then, based upon the resulting objective function and its derivatives, updating the parameter values until the objective function is converged to a global minimum (Fig. 2a). The derivatives required for the minimization of the objective function can be calculated either by numerical differentiation or by formulating an adjoint problem (Haslinger and Mäkinen 2003). The latter, however, becomes complicated for problems with inequality-type constraints, which appears in the form of leaflet contact in the current situation. On the other hand, numerical differentiation using finite difference can be performed simply by evaluating the cost function at perturbed parameter values. Therefore, we adopted the finite difference numerical differentiation in the present approach because of its simplicity in implementation. During the simulation of forward model and calculation of objective function, the following data are used as an input: (1) leaflet-deformed shape, (2) reference geometry, (3) fiber architecture and (4) load and boundary conditions. More mathematical details of the current framework are presented next, with details of the forward model described first, followed by those of the inverse modeling setup.

2.4 Mathematical formulation of the forward model

As we assume that the most critical functional properties of heart valves are related to their tensile stresses and not bending stresses, we focus on the closing phase only, since it is when the highest tensile stresses occur, providing the largest range of deformation. It has been shown that during the closing phase, i.e., after the leaflets are in contact, deformation of the leaflet is relatively insensitive to the fluid model (Kamensky 2015). In other words, the in-plane deformations of leaflets during valve closure are accurately captured from a biosolid mechanics approach. Thus, we considered this problem from a structural point of view only, not considering the fluid flow and simulating only closing phase of the cardiac cycle by applying normal pressure load on the valve leaflets. The simulation was performed in two ways—(1) all the leaflets modeled simultaneously with explicit contact between each pair of leaflets modeled as contact between two deformable bodies and (2) each of the three leaflets modeled in isolation, with other leaflets idealized by symmetry planes that are modeled as rigid walls located at $\pm 60^\circ$ of the leaflet's plane of symmetry. All other settings and parameters were kept the same for the above two types of simulations. The leaflets are functionally elastic; hence, the forward problem of valve closing becomes a hyperelasticity problem with contact constraints.

Fig. 2 **a** Overall inverse modeling framework: the forward model is put in a loop, where we start with guess mechanical properties, compute the cost/objective function and its derivatives, and then accordingly update the material parameters until convergence. Note the input required for such framework (oval shaped). **b** In the third and fourth steps of the algorithm, projection calculation involves evaluating the normal of the closest quadrilateral element and using that to find the projection point



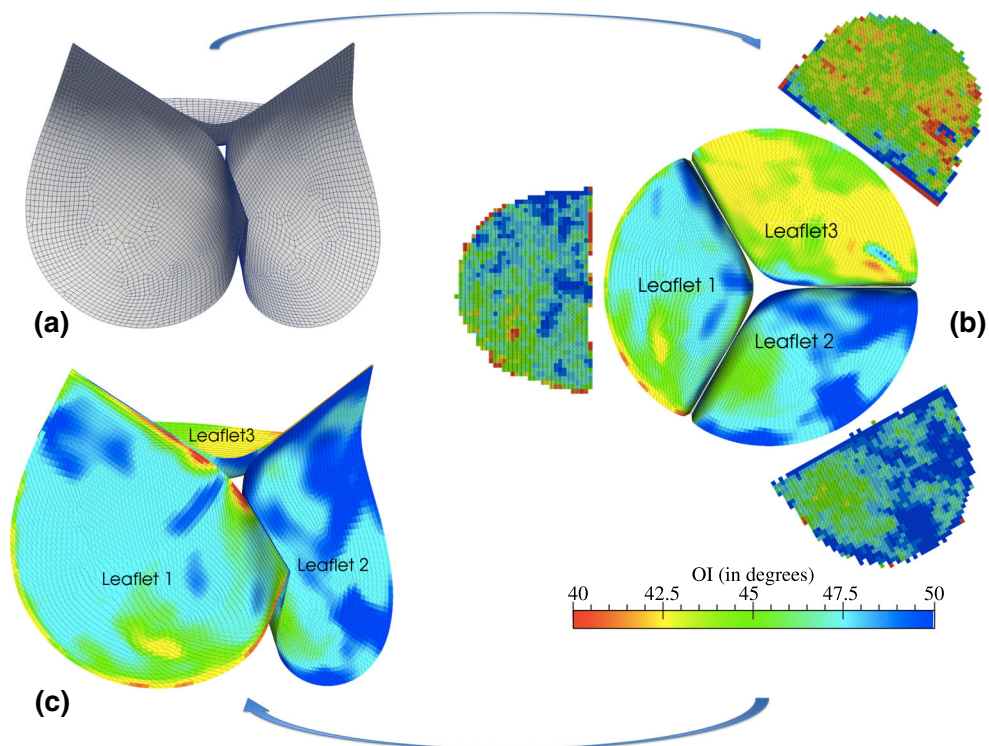


Fig. 3 Quadrilateral mesh used for computations (a), the fiber structure of three leaflets measured experimentally and then mapped onto valve geometry using spline technique (b), another view of the final valve mesh with fiber structure (c)

2.4.1 Finite element discretization

The forward problem of valve closing was implemented in FEBio (Maas et al. 2012), with valve leaflets modeled using Reissner–Mindlin thin shell elements formulated using extensible director approach (Betsch et al. 1996). The shape of the valve was taken from the previous study (Sun and Sacks 2005) in the form of a quadrilateral meshed geometry file, where each leaflet was made up of 1025 cells and 1082 nodes. To improve the refinement as well as quality of elements (measured in terms of the aspect ratio and the smallest angle of the polygon), the geometry was imported into Hypermesh and remeshed so that each leaflet was made up of 2789 cells and 2880 nodes (Fig. 3a). Leaflets were discretized using four-node quadrilateral elements, with each node assigned six degrees of freedom (three for translation and three for rotation). Therefore, the complete discrete version of the model had 51,840 degrees of freedom. The displacement was interpolated using bilinear shape functions, and a constant thickness was assigned to each leaflet as measured during the experiment (Table 1). The stresses were integrated through the shell thickness using three point Gauss quadrature rule to obtain bending moments.

The fiber architecture, determined for each flattened leaflet in the form of preferred fiber direction θ_0 and fiber splay OI (Fig. 3b), was borrowed from (Sun et al. 2005). Next,

to register these two-dimensional fiber structure maps onto the three-dimensional valve shape, a spline-based technique, that we have previously developed (Aggarwal et al. 2013, 2014), was used (Fig. 3b, c). The standard deviation (σ) of orientation distribution function (ODF) Γ is related to OI through the following relation:

$$\int_{-\text{OI}/2}^{\text{OI}/2} \Gamma(\sigma, \theta) d\theta = 0.5 \quad (1)$$

Γ was approximated herein as a Gaussian distribution symmetrically centered at preferred direction θ_0 (Fan and Sacks 2014) with more details provided in Sect. 2.4.3.

2.4.2 Loads and boundary conditions

Nodes at the basal attachment were assigned a zero-translation boundary condition to match the experimental conditions. The rotational degrees of freedom were not fixed, thus representing a pinned-type boundary. The pressure head was simulated using a normal pressure to the surface. It increased linearly from 0 to 120 mm of Hg in 0.6 s. To be noted is that the simulation time of 0.6 s is “pseudo-time” and was, thus, arbitrarily chosen; since the equilibrium equations are satisfied at every load/time step, the loading

Table 1 Summary of the in vitro experimental dataset borrowed from (Sun and Sacks 2005) for developing the current framework

Valve image	Leaflet 1 (129 points)	0 mm of Hg 40 mm of Hg 80 mm of Hg 120 mm of Hg
	Leaflet 2 (125 points)	0 mm of Hg 40 mm of Hg 80 mm of Hg 120 mm of Hg
	Leaflet 3 (118 points)	0 mm of Hg 40 mm of Hg 80 mm of Hg 120 mm of Hg
Fiber structure*	Leaflet 1 Leaflet 2 Leaflet 3	OI and θ_0 OI and θ_0 OI and θ_0
Biaxial stress–strain data	Leaflet 1 Leaflet 2 Leaflet 3	Seven parameters in Fung's law Seven parameters in Fung's law Seven parameters in Fung's law
Leaflet thickness [§]	Leaflet 1 Leaflet 2 Leaflet 3	0.518 mm 0.487 mm 0.457 mm

* Spatially varying over the leaflets at a grid spacing of 256 microns

§ Average of five points

rate is infinitesimal. This was also the case in the experiment, where only a static pressure head was applied. Thus, a quasi-static formulation was utilized by ignoring inertial effects. The total time of pressure application was chosen arbitrarily and does not affect the results (given that all the time step parameters of simulation are changed proportionately).

2.4.3 Constitutive model

A structural model was used (Abelev et al. 2013) for two main reasons: (1) It allowed us to fully utilize the fiber architectural information in the form of point-wise orientation distribution function and capture the coupling between response along different directions, and (2) it reduced the number of parameters to be estimated per leaflet to only two, as will be seen below. Although Fung-type elastic model, which was used in (Sun et al. 2005), can incorporate preferred fiber direction through the material axes definition, it is not possible to incorporate any fiber distribution information. Furthermore, in a Fung's model the convexity of cost function can be lost, creating problems with the convergence and uniqueness of the solution. This is consistent with the previous work where Fung-based strain energy function was shown to be non-convex in unconstrained parameter space (Sun and Sacks 2005).

The structural model describes the strain energy density function in terms of each individual component—the matrix and fibers. Here, we combine all the fibers together into a single family, so that total strain energy is the sum of fiber and matrix parts:

$$\Psi(\mathbf{C}) = \Psi_f + \Psi_m. \quad (2)$$

Here, the volume fractions of each part have been ignored because they are assimilated into the material constants. Although incompressibility is a widely used approximation for soft tissue mechanics, it is known to cause numerical convergence issues. Therefore, to determine the effect compressibility has on the numerical stability and inverse modeling results, a compressible neo-Hookean model was used for the matrix part:

$$\Psi_m = \frac{\mu}{2} (I_1 - 3) - \mu \ln J + \frac{\bar{\lambda}}{2} (\ln J)^2 \quad (3)$$

where $I_1 = \text{tr}(\mathbf{C})$ is the first invariant of right Cauchy–Green strain tensor \mathbf{C} , $J = \sqrt{\det(\mathbf{C})}$ is the ratio of deformed to initial volume, and the two Lamé constants ($\bar{\lambda}$ and μ) are estimated from the small strain limit elastic constants (Young's modulus \bar{E} and Poisson's ratio ν) using the relations:

$$\begin{aligned}\bar{\lambda} &= \frac{\bar{E}\nu}{(1+\nu)(1-2\nu)} \\ \mu &= \frac{\bar{E}}{2(1+\nu)}.\end{aligned}\quad (4)$$

The above material model for matrix becomes incompressible in the limit $\bar{\lambda} \rightarrow \infty$ or equivalently $\nu \rightarrow 0.5$. The fiber part is calculated by integrating over the fiber ensemble responses in all the directions. That is,

$$\Psi_f = \int_{\theta} \Gamma(\theta) \Psi^{\text{ens}} (\mathbf{N}^T \cdot \mathbf{E} \cdot \mathbf{N}) d\theta \quad (5)$$

where \mathbf{N} is the vector along fiber direction in the reference configuration, $\mathbf{E} = \frac{1}{2}(\mathbf{C} - \mathbf{I})$ is the Green–Lagrange strain tensor, and $\Gamma(\theta)$ is the fiber orientation distribution function, which for pericardium has been shown to be the superposition of normal and uniform distributions (Fan and Sacks 2014):

$$\Gamma(\theta) = d_e \frac{1}{P} \exp\left(-\frac{(\theta - \theta_0)^2}{2\sigma^2}\right) + \frac{(1-d_e)}{\pi}. \quad (6)$$

Here, the first term signifies the normalized Gaussian distribution and the second term is a uniform distribution. Accordingly, $d_e \in [0, 1]$ is the anisotropy parameter and P is the normalizing factor

$$P = \int_{-\pi/2}^{\pi/2} \exp\left(-\frac{(\theta - \theta_0)^2}{2\sigma^2}\right) d\theta = \sqrt{2\pi}\sigma \operatorname{erf}\left(\frac{\pi}{2\sqrt{2}\sigma}\right). \quad (7)$$

It should be noted that we do not use the structural tensor approach to describe fiber distribution due to its potential to loose coupling information (Cortes et al. 2010). All the components of the fiber distribution function $\Gamma(\theta)$ are determined directly from the experimentally obtained and mapped fiber architecture data. In present formulation, to avoid extremely high computational times, a simplified model was used (Fan and Sacks 2014), where the ensemble response is approximated as an exponential function:

$$\Psi^{\text{ens}}(E_{\text{ens}}) \approx (c_0 \left(\frac{e^{c_1 E_{\text{ens}}}}{c_1} - 1 \right) - c_0/c_1) \quad (8)$$

where $E_{\text{ens}} = \mathbf{N}^T \cdot \mathbf{E} \cdot \mathbf{N}$ is the ensemble strain, and c_0 and c_1 are two material parameters. This model has been shown to capture the mechanical behavior of pericardium extremely well (Fan and Sacks 2014). In its original form (Fan and Sacks 2014), the model included a terminal stiffness, i.e., the stiffness becomes constant after a limit strain. However, we found that the upper limit

proved to be higher than the strains encountered during valve closure and, thus, was considered unnecessary. We observe that c_0 has units of stress, while c_1 is dimensionless.

The matrix stiffness for crosslinked bovine pericardium was previously estimated to be $\bar{E} = 200$ kPa (Mirnajafi et al. 2005), and the Poisson's ratio was varied from $\nu = 0.30$ to 0.49 to determine the sensitivity with respect to compressibility. For numerical computations of the integral over fiber directions in Eq. (5), Gauss quadrature rule was utilized. Accordingly:

$$\begin{aligned}\Psi_f &= c_0 \int_{\theta} \Gamma(\theta) \left(\frac{e^{c_1(\mathbf{N}^T \cdot \mathbf{E} \cdot \mathbf{N})}}{c_1} - \mathbf{N}^T \cdot \mathbf{E} \cdot \mathbf{N} \right) d\theta \\ &\approx c_0 \sum_{i=1}^n \Gamma(\theta_i) \left(\frac{e^{c_1(\mathbf{N}^T \cdot \mathbf{E} \cdot \mathbf{N})}}{c_1} - \mathbf{N}^T \cdot \mathbf{E} \cdot \mathbf{N} \right) w_{\theta_i}.\end{aligned}\quad (9)$$

A comparison of various orders of the Gauss quadrature rule was made, and it was concluded that using a 10-point Gauss quadrature (exact up to a polynomial of 19th order) gave an accurate result (for the range of σ in current problem) while keeping the computational costs reasonable. We note that although it is possible to approximate the above integral with a closed-form solution (Raghupathy and Barocas 2009), these methods restrict the choice of ODF without providing substantial performance improvements. This material model was implemented using plug-in capability of FEBio. For the summation in (9), the directions and $\Gamma(\theta)$ were pre-computed and stored, making the computational cost around only 2–3 times more expensive than the conventional closed-form constitutive laws (e.g., neo-Hookean).

2.4.4 Contact constraint implementation

The contact between leaflets was modeled explicitly using augmented Lagrange multiplier method (Wriggers and Laursen 2007). This was chosen over the usual quadratic penalty method because of the importance and range of contact forces in this situation. During valve closing, the contact forces become fairly high, thus requiring large penalty parameter which made the problem ill-conditioned. To solve this problem, an augmented Lagrange multiplier method with a penalty parameter of 0.1 MPa in the normal direction was used instead. A minimum of three augment iterations were enforced with the convergence criterion on Lagrange multiplier and the gap tolerance. For Lagrange multiplier χ , the convergence was defined as

$$\frac{\|\Delta \mathbf{x}\|}{\|\mathbf{x}_k\|} < 0.01, \quad (10)$$

and for gap between the leaflets a root-mean-square overlap of less than 0.01 mm was deemed as converged. After 10 augment iterations, the solution at current load was assumed to be converged irrespective of the gap and Lagrange multiplier values, and simulation was continued onto the next time step. For the tangential direction of contact surfaces, high enough frictional coefficient was used to prevent unnecessary slipping ($\mu_f = 0.1\text{--}10$). To enforce the frictional force, a frictional penalty of 0.1 MPa was used in the augmented Lagrange formulation.

2.4.5 Simulation and convergence parameters

To simulate the entire closing of the valve, an adaptive time stepping technique was used. A constant minimum time step of $\Delta t_{\min} = 4 \times 10^{-4}$ s was chosen after an exhaustive convergence analysis. The maximum time step Δt_{\max} was increased linearly during the simulation from 4×10^{-4} at zero pressure to 8×10^{-3} at a pressure of 40 mm of Hg, and was kept constant from there on. The automatic time step control was based upon the number of iterations required for convergence in the previous step. This time stepping arrangement provided a small enough time increment for the solution to be stable, but large enough for the simulation to complete in a reasonable time. Quasi-Newton method-based LBFGS algorithm was used for iteratively solving the equilibrium equations at each load step (Liu and Nocedal 1989). For this algorithm, the stiffness matrix was calculated exactly in the first iteration and then updated in an approximate way during search iterations. To solve the linear system of equations thus formed, we utilized the Pardiso solver with a single processor (Schenk and Gartner 2004). For each load step, the solution was iterated until convergence defined in terms of the displacement and energy changes (both needed to be satisfied). For displacement vector \mathbf{U} , the convergence criterion was defined as

$$\frac{\|\Delta \mathbf{U}\|}{\|\mathbf{U}_{k+1}\|} < 0.01, \quad (11)$$

and for the changes in total energy of the system E, the convergence criterion was defined as

$$\frac{|\Delta E|}{E_{k+1}} < 0.01. \quad (12)$$

2.5 Computational details of the inverse model

The Forward Model described in the previous section was controlled and run through an in-house developed python wrapper for inverse modeling setup. Marker positions at

four pressure levels from the experimental data were used as an input to the inverse model. The point cloud data provided by the experimental technique (Sect. 2.2) for different leaflets would, in general, be in a different coordinate system than the geometry. To solve this issue, Iterative Closest Point algorithm (Besl and McKay 1992) implemented in VTK library (Schroeder et al. 1998) was used to align the point cloud at zero transvalvular pressure with the valve geometry through rigid body registration. Then, the same transformation was applied to point cloud at the rest of the pressure levels.

Choice of the objective function is a critical aspect of inverse modeling setup. In order to be consistent with the clinical imaging modalities, which provide only the shape without any information about material points, we *did not use* the information from the experimental data on the material points. Instead, the points were used only to describe valve shape, and we focused on matching the shape of the leaflet surface. That is, the objective cost function was defined as the difference *in shape* of the deformed mesh and that of the experimental data points. The difference was calculated along the normal direction of deformed mesh. Thus, it can be defined mathematically as

$$\mathcal{F} = \sqrt{\sum_{i,\alpha} \|\mathbf{x}_i^\alpha - \tilde{\mathbf{x}}_i^\alpha(c_m)\|^2} = \sqrt{\sum_{i,j,\alpha} (x_{ij}^\alpha - \tilde{x}_{ij}^\alpha(c_m))^2}. \quad (13)$$

The summation is performed over data point number $i = 1\text{--}m$, direction $j = 1, 2$ and 3 , and time frame (or pressure level) $\alpha = 1$ to number of available states (maximum 3 here).

For calculating the projection points, the following algorithm was used. We start by assuming a given experimental point \mathbf{x}_i^α and deformed mesh, which is a union of piecewise flat quadrilateral elements, $M = \bigcup_j \Theta_j(\mathbf{v}_{1j}, \mathbf{v}_{2j}, \mathbf{v}_{3j}, \mathbf{v}_{4j})$. Here, \mathbf{v}_{kj} are the four ($k = 1\text{--}4$) vertices of the quadrilateral j . To determine the projection point $\tilde{\mathbf{x}}_i^\alpha \in M$, the steps of algorithm are:

1. Determine the centroids of all quadrilateral elements

$$\bar{\mathbf{v}}_j = \frac{1}{4} \sum_{k=1}^4 \mathbf{v}_{kj}$$
2. Determine the closest element centroid $\hat{j} = \arg \min_j \|\mathbf{x}_i^\alpha - \bar{\mathbf{v}}_j\|$
3. For the element \hat{j} , calculate its normal vector $\mathbf{n} = (\mathbf{v}_{2\hat{j}} - \mathbf{v}_{1\hat{j}}) \times (\mathbf{v}_{3\hat{j}} - \mathbf{v}_{1\hat{j}})$
4. Determine the projection point using normal vector $\tilde{\mathbf{x}}_i^\alpha = \mathbf{x}_i^\alpha - [\mathbf{n} \cdot (\mathbf{x}_i^\alpha - \bar{\mathbf{v}}_{\hat{j}})] \mathbf{n}$ (Fig. 2b)

5. Check if the projection point lies within the element using the condition that sum of angles \tilde{x}_i^α makes with four edges of quadrilateral is equal to 2π
6. If it lies inside the quadrilateral, it is the final projection point
Else, determine the projection point on each of the edge of quadrilateral $\Theta_{\hat{j}}$
7. If any of those projection points lies inside the corresponding edge, it is the final projection point
Else, the closest vertex out of $(v_{1\hat{j}}, v_{2\hat{j}}, v_{3\hat{j}}, v_{4\hat{j}})$ is approximated as the final projection point. That is $\arg \min_k \|x_i^\alpha - v_{k\hat{j}}\|$

To minimize the cost function(13), a Levenberg–Marquardt algorithm was used, which defines the change in parameters Δc_m as

$$(\mathbf{J}^T \mathbf{J} + \lambda \text{diag}(\mathbf{J}^T \mathbf{J})) \Delta c_m = \mathbf{J}^T [x_{ij}^\alpha - \tilde{x}_{ij}^\alpha(c_m)]. \quad (14)$$

The derivatives of the cost function $[\mathbf{J}]_{ij,m} = \partial \tilde{x}_{ij}^\alpha(\hat{c}_m) / \partial c_m$ were calculated using central finite difference by perturbing each of the parameters by 1% above and below its current value. The value of λ was kept constant at a value of $\lambda = 5$ since it provided a balance between the stability and convergence speed of the algorithm. The simulations were run on Texas Advanced Computing Center (TACC) on a single node with 12 processors. The finite difference cases for cost function derivatives were run in parallel using multiprocessing module of python wrapper. Therefore, for n parameters to be determined, this setup required a total of $2n+1$ simulations in parallel, each of them running on a single processor.

Table 2 Summary of cases analyzed

Case	Parameter varied	Values used
(a) Number of frames of imaging and corresponding pressures	Pressure levels	(1) 40 mm; 80 mm; 120 mm; (2) 40, 80 mm; 40, 120 mm; 80, 120 mm; (3) 40, 80, 120 mm
(b) Simulation parameters	Poisson's ratio ν Friction coefficient μ_f Matrix stiffness \bar{E}	0.35; 0.49 0.5; 1; 5 100 kPa; 200 kPa; 300 kPa
(c) Contact	Explicit contact Individual leaflets	Composite valve Leaflet # 1; 2; 3
(d) Fiber architecture	Fiber splay σ Fiber preferred direction θ_0	Uniform 0.58 (average); 0.5; 0.8 radians Mapped; Circumferential
(e) Image resolution	Added noise to point cloud	Random (Gaussian with standard deviation of 0.2 mm); Systematic (Table 3)

2.6 Analysis and comparison of different cases

In order to thoroughly analyze current framework, we started by analyzing the properties of the objective cost function, e.g., its convexity and sensitivity. We exploited the fact that the cost function has only two parameters by visualizing it as a surface. Details of this analysis and the cases calculated are presented next (Sect. 2.6.1). Once the properties of the cost function were established, minimization was carried out to obtain resulting parameters using current framework (Sect. 2.6.2). Using these resulting parameters, verification and validations studies were carried out (Sect. 2.7).

2.6.1 Cost function analysis

Several cases were computed for varying material and simulation parameters, which are summarized in Table 2. For each case, cost function (13) was evaluated for a range of mechanical parameter values (c_0 and c_1). The range of parameters (c_0 from 0.1 kPa to 100 kPa and c_1 from 20 to 80) was chosen after a careful experimentation of the current framework. The objective function, being a function of two variables, was plotted both as a surface in three dimensions and a contour in two dimensions to visualize its shape and the location of minima. To compare any two cases, either these surfaces were compared directly, or the difference between the two functions was calculated and plotted as a surface. Specifically, the following cases were analyzed.

- (a) The effect of using different combinations of the frames from experimental point cloud data was estimated by directly comparing these surface plots for various cases. The case where all three pressure levels were used was named as the “base” case.

- (b) Differences in the objective function were calculated by perturbing various simulation parameters—the Poisson's ratio, the frictional coefficient between the leaflets, and the stiffness of the matrix part in constitutive model.
- (c) To determine the importance of explicit contact, single-leaflet simulations were compared against the composite leaflet simulation.
- (d) To study the importance of incorporating fiber structure, the fiber splay σ and fiber direction θ_0 were varied. The point-wise fiber splay determined from ex vivo experiment was replaced by an average value (0.58 radians) and then was perturbed above (0.8 radians) and below (0.5 radians). The effect of each variation was visualized as a surface plot of the difference between the cost functions. For determining the effect of fiber direction, it was not possible to average because of the high variability in pericardium tissues of bioprosthetic valve leaflets. Instead, the leaflet-specific mapped fiber directions (obtained experimentally) were replaced by a generic circumferential fiber direction, and the cost function was reevaluated. The difference in the cost function compared to the base case was plotted as a surface.
- (e) To determine the effect of imaging resolution and noise, an artificial noise was added to the point cloud and the cases were reevaluated. To differentiate the random noise and systematic error, two cases were evaluated. First, a random Gaussian noise with a zero mean and standard deviation of 0.2 mm was added to the point cloud coordinates. This value of the standard deviation was chosen based upon the current resolution of 3D ultrasound imaging technology. Secondly, a systematic error was introduced that varied leaflet to leaflet but was constant on each leaflet. These systematic error values are shown in Table 3. For each of these cases, the differences were determined in the form of change in the cost function, as well as the shift in minima of cost function.

2.6.2 Minimization and analysis of the final surface fit

Minimization was performed with three distinct starting points chosen from different regions of the parameter space. Results were considered converged when the absolute change in parameters was less than 1 %. Two cases were analyzed: 1) When all three leaflets were assigned same mechanical parameters and 2) when the three leaflets were allowed to have different mechanical parameters (however homogeneous on each of them). To analyze the final surface fit, the *signed* projection distances $[\mathbf{x}_i^\alpha - \tilde{\mathbf{x}}_i^\alpha (c_m)]$ at converged set of parameters were calculated. The *signed* distance here means that a positive sign was assigned if the point was on one side of the leaflet (ventricle side), and negative was assigned if it was on the other (aorta side). Arithmetic means and standard deviations were calculated for both signed and absolute projection

Table 3 Uniform error imposed on three leaflets to evaluate the sensitivity to systematic image noise

Leaflet	Pressure (mm)	Δx	Δy	Δz
1	40	0.06	0.27	0.1
	80	0.03	0.38	0.19
	120	0.03	0.48	0.16
2	40	0.10	0.24	0.32
	80	0.19	0.27	0.14
	120	0.25	0.33	0.26
3	40	0.02	0.14	0.02
	80	0.05	0.1	0.01
	120	0.01	0.14	0.02

distances. The absolute projection distance (which also acts as error in the cost function definition) was plotted on the triangulated point cloud.

2.7 Verification and validation studies

It was observed that strain path applied during ex vivo biaxial test experiment was significantly different from the one that leaflets undergo during valve closure. This leads to difficulties in comparison of results. Furthermore, direct comparison of parameters in exponential-type inverse model was found to be deceptive. Therefore, for verification and validation, a direct comparison was made through calculation of stress-strain response during biaxial stretch protocol.

2.7.1 Biaxial simulations

To simulate the biaxial experiment, a 3.33 mm \times 3.33 mm tissue sample from the center of each leaflet was used. This tissue represents the position of markers placed at the inner third of the 10 mm \times 10 mm sample used during the biaxial experimental setup. For high fidelity, mapped fiber structure was used to define the fiber direction and splay, which varied point-wise over the sample. This is not possible with the standard parameter fitting to biaxial data, where the calculations are done at the center of the sample, and, thus, a constant fiber structure has to be assumed. Strains measured in the experiment during equi-biaxial stress protocol were used to apply displacement boundary conditions on the sample. The time step and convergence conditions were kept the same as in the main simulation. Final reaction forces evaluated on the edges of the sample were used to calculate the stresses and strain energy in the leaflet at chosen set of mechanical parameters.

2.7.2 Verification

For verification of the numerical implementation, a synthetic dataset was generated at representative values of

$\bar{c}_0 = 11.539$ kPa and $\bar{c}_1 = 36.43976$.¹ Projections of the marker positions used in in vitro study to the reference geometry of valve leaflets were converted into “virtual markers” so that the density of markers remains the same. To generate synthetic point cloud at different pressures, a forward simulation was run using these known parameter values of \bar{c}_0 and \bar{c}_1 , and the virtual markers’ positions were calculated at 40, 80 and 120 mm of Hg transvalvular pressure. Then, using the inverse modeling setup, the parameters c_0 and c_1 were estimated based on these virtual marker positions. Biaxial test was simulated on all three leaflets using the original (\bar{c}_0 and \bar{c}_1) and estimated (c_0 and c_1) values of mechanical parameters. At the end the stress–strain curves were compared from two set of parameter values.

2.7.3 Validation

For validation of our approach against experimental results, we compared the strain energies density during equi-biaxial test protocol. We have previously shown that comparing strain energy density is equivalent to comparing stress–strain response (Sacks and Chuong 1998), and being a scalar measure, makes it easier to get a sense of the overall response in a 2D graph. First using the in vitro point cloud dataset, the objective function (13) was minimized to obtain the mechanical parameters via our inverse modeling framework. These parameter values were used to simulate the biaxial testing setup as described above and strain energy density was calculated as a function of the applied strain. Strains were used to directly calculate the experimental strain energy density by using Fung’s transverse isotropic constitutive law and the associated seven parameters reported in (Sun et al. 2005)—that is, by directly plugging-in the applied strain into the Fung-type strain energy relation used in (Sun et al. 2005). The two strain energy density curves were plotted for all three leaflets as a function of the applied strain and compared to validate our approach.

3 Results

3.1 Forward model

Using our forward model, closing of the valve could be simulated at any given set of mechanical parameter values. Example deformed shape and leaflet stresses in the valve using parameters $c_0 = 11.539$ kPa and $c_1 = 36.43976$ thus

¹ These values of the parameters were taken from a crosslinked pericardium tissue sample tested in our laboratory. However, we must impress that the results presented in the verification section do not depend at all upon the choice of these parameters; we have tested for multiple values and found similar agreement in all of the cases. Here we provide only one case for demonstration purpose.

obtained are shown (Fig. 4). Even when all of the simulation parameters, including c_0 and c_1 in the constitutive equation, were kept identical for the three leaflets, each leaflet undergoes different deformations and stresses. This was attributed to the varying fiber architecture, and thus demonstrates the importance of point-wise mapped fiber structure. Also, to be noted is that mesh density is fine enough to capture the stress concentrations at leaflet commissure points and, thus, accurately define leaflet deformation. The apparent gap between the leaflets is because they are visualized using mid-plane as a membrane, and therefore, the gap is due to the physical thickness of the leaflets. Each forward model run took approximately 35–40 min on a single processor.

Despite using carefully chosen simulation parameters, some minor convergence problems were encountered in a small number of cases. This was expected because of the high nonlinearity of the structural model, where the local tangent modulus increases with strain, thus possibly making the stiffness matrix ill-conditioned. The nonlinearity of this problem was further enhanced due to contact constraints, giving rise to numerical instabilities in some situations. It was observed that in approximately 3–4 % of the cases the simulations failed to converge purely because of numerical issues. In such a situation, the mechanical parameter values (c_0 and c_1) were perturbed by a randomly chosen small amount (between –3 and 3 %) and the simulation was run again.

3.2 Verification of inverse model

To verify our numerical implementation, the cost function evaluated using synthetic point cloud dataset is plotted as a surface (Fig. 5a) and as a contour (Fig. 5b). The set of *original* mechanical parameters used to generate this dataset (indicated using red circle) lies at the bottom of the cost function. The objective function is clearly convex everywhere and has a unique minima, thus satisfying one of the primary criterion of inverse modeling setup. Although, the actual minima and solution is unique, we also observe that the lowest part of the cost function is very close to being flat. This was found to be a property of the exponential form of the ensemble response function (8) and is analyzed analytically by using an isolated exponential function (see Appendix 6). A closed-form equation for the lowest region or the banana-shaped curve, which we will refer to as the “iso-stress-strain minima” region (for reasons that will become clear in Sect. 3.3), is obtained analytically (17). This curve, for *original* parameter values, $\bar{c}_0 = 11.539$ kPa, $\bar{c}_1 = 36.43976$ and $\epsilon = 0.1$, is plotted as a solid blue line (Fig. 5b), which matches precisely with the iso-stress-strain minima of the contour plot. Furthermore, it is noted that the minima of the cost function resembles the error function from constitutive model (Sacks 2000b). This

Fig. 4 Example displacement (left) and stress profiles (right) at fully loaded state. Note the heterogeneity and the slight asymmetry in deformation even though all the mechanical parameters except fiber structure are same for the three leaflets. The forward model correctly captures the coaptation region and stress concentrations at the commissure points

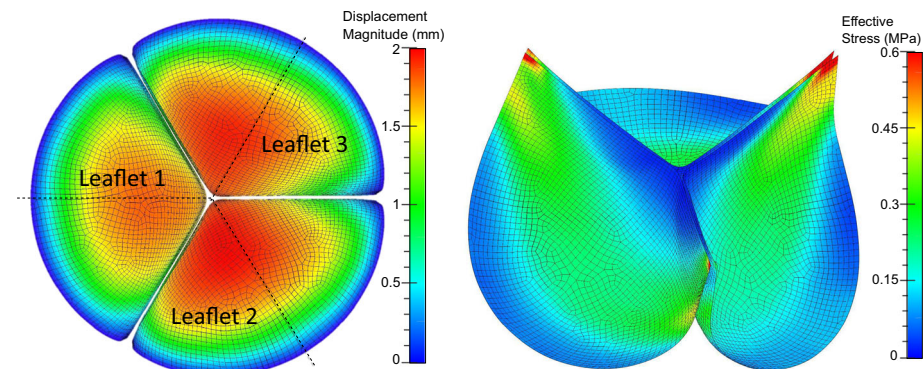
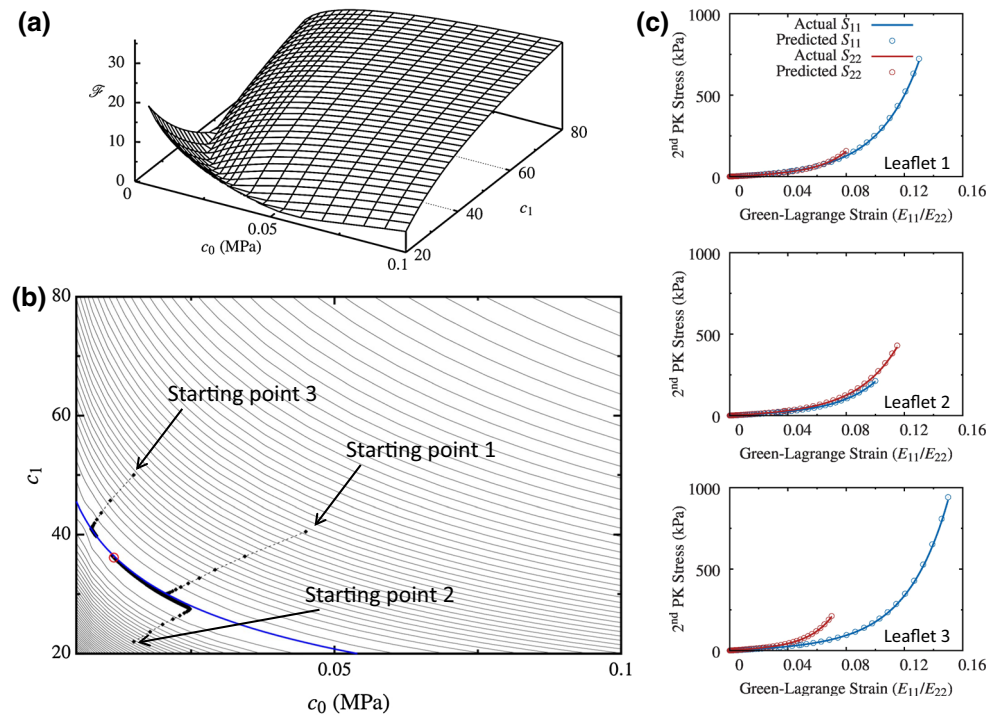


Fig. 5 Surface plot (a) and contour plot (b) of the cost function for synthetic data. In (b) the red circle represents the original parameters and dashed lines indicate three minimization sequences with different starting points—all of them converging to the red circle showing uniqueness of the solution. The solid blue line is the plot of analytical form of the c_0^{\min} (17). c The comparison of stress-strain behavior during biaxial testing of three leaflets using parameters obtained from inverse model (circles) and from original parameters (solid line)



signifies that although the valve is loaded under normal pressure, locally it still behaves like a planar membrane under biaxial load.

During the minimization procedure (indicated using dashed black line with dots, Fig. 5b), the iterations converge to the absolute minima irrespective of the starting guess again emphasizing the uniqueness of our solution. Since the iso-stress-strain minima region is close to flat, the variation of cost function along that curve is extremely small, leading to a slow convergence once solution approaches that region. The final results of the inverse model are also verified by plotting the effective stress-strain relationship during biaxial testing protocol at both the original and predicted values of c_0 and c_1 (Fig. 5c). The original (solid line) and predicted (open circles) results match extremely well, thus, verifying the numerical implementation. It was observed that introduction of small noise into the input synthetic point cloud data caused the

absolute minima of the cost function to shift along the blue line; however, the effective stress-strain behavior remained very similar to the original case. This point is further investigated next using the real marker positions from in vitro dataset.

3.3 Sensitivity to number of loading states

From the pressure levels at which the valve was imaged (i.e., 40, 80 and 120 mm of Hg), different combinations can be chosen in our framework while constructing the objective cost function (13). Cost function is evaluated using actual marker positions from the in vitro dataset, and by using all possible combinations of loading states from the experimental data (Fig. 6). The lowest region of the cost function ($\mathcal{F} - \mathcal{F}_{\min} = 1$ mm) is colored to emphasize its convexity. If only one frame is used, the size of the low-

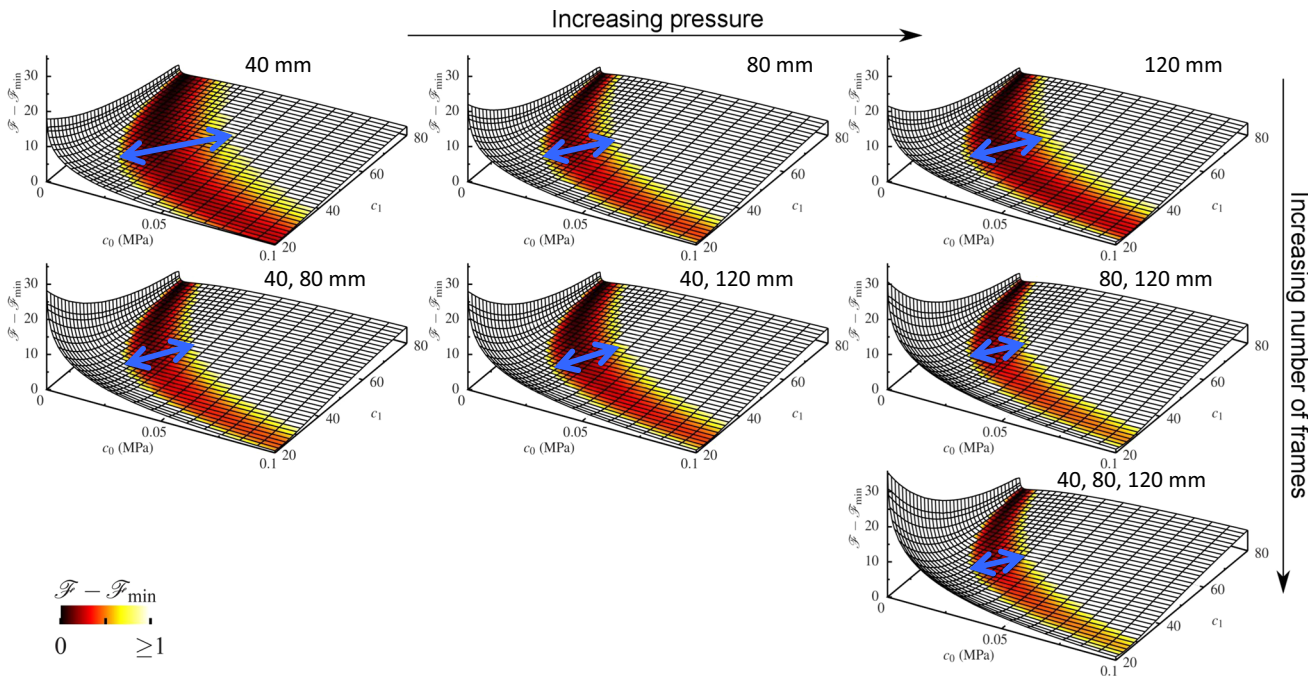


Fig. 6 Cost function using all possible combinations of pressures frames for the base case. The lowest 1-mm region is colored to emphasize convexity. The double-headed blue arrow indicates the width of the

lowest region for each case. Notice change in the size of that region as pressure and number of frames are increased, which is related to the variability and confidence in the final results

est colored region shrinks as the pressure is increased from 40 to 80 and to 120 mm of Hg (Fig. 6 top row). Also, as the number of frames used is increased, the colored region shrinks further. Here, the colored region is used as an indicator of the confidence in the final results. Therefore, the result with highest confidence is obtained when we use all three pressure levels (bottom right plot Fig. 6), and this case will be referred to as the “base” case in rest of the analysis.

Similar to the case with synthetic dataset, we observe a long J-shaped region that contained only small magnitude variations in the cost function. Choosing different $c_0 - c_1$ pair of values from this region yielded very similar effective stress-strain responses (Fig. 7a). Thus, we named this region as the “iso-stress-strain minima” region or curve. On the other hand, changing the $c_0 - c_1$ values orthogonal to this curve gives drastically different stress-strain responses (Fig. 7b). This result underscored that parameters in nonlinear models often cannot be compared individually, but rather how they work within the nonlinear model to produce the effective end result. Additionally, since the cost function value remains almost constant along this “iso-stress-strain minima” curve, any small perturbation or noise in the input data could shift the absolute global minima of the cost function along this curve changing the parameter values. However, the effective stress-strain response would remain the same (Fig. 7a). Henceforth, we focus on the effective

stress-strain response as the result of our framework rather than final parameters values, and the corresponding variations are visualized using deviations in the iso-stress-strain minima curve.

3.4 Importance of modeling explicit contact

Instead of simulating the intact valve (with all three leaflets) with explicit contact, simulating a single leaflet with symmetric wall boundary improved the computational cost substantially. Specifically, a single-leaflet forward simulation took 2–3 minutes as opposed to 35–40 min for the explicit contact simulation. Therefore, we explore this option to find out if single-leaflet simulations can be utilized to gain a computational speedup. The cost function shapes evaluated for three individual leaflets using all three frames are plotted—both for composite valve simulation using explicit contact and single valve simulations using symmetric rigid wall constraint—and the results using these two approaches are very close (Fig. 8).

The differences between two cases (Fig. 8 rightmost column) are almost zero except in some regions indicating a weak coupling between the three leaflets as far as our objective function is concerned. As a result, single-leaflet simulations can be used to obtain an initial estimate of the parameters followed by composite valve (all-leaflet) simulations, thus significantly reducing the computational cost.

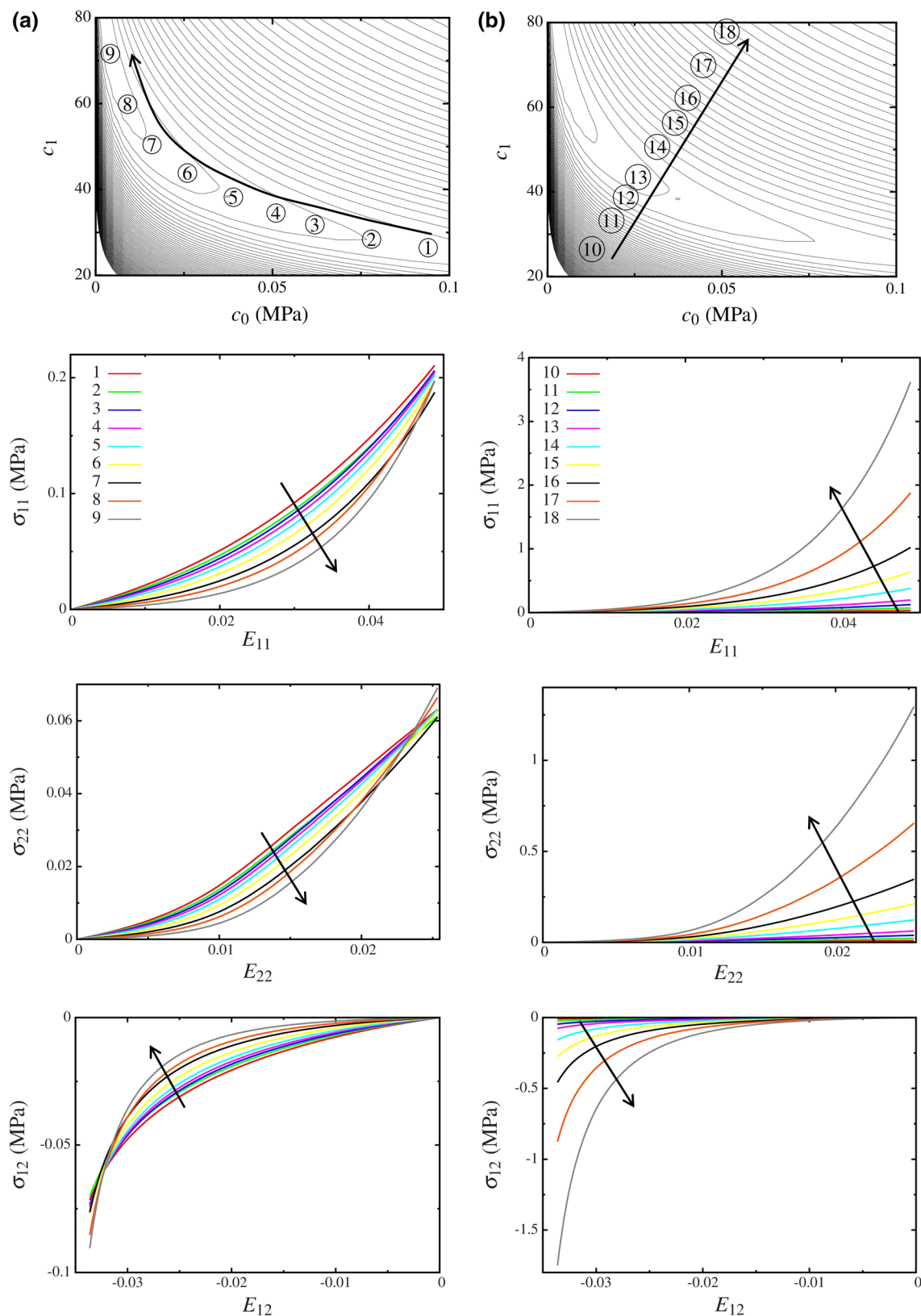


Fig. 7 Stress–strain curves at different parameter values (c_0 and c_1) along the banana-shaped minima region of cost function (a) and across it (b). Along the minima region, the differences are minimal even for

substantial change in parameter values; however, across the minima region, responses vary widely for even small changes in the parameter values

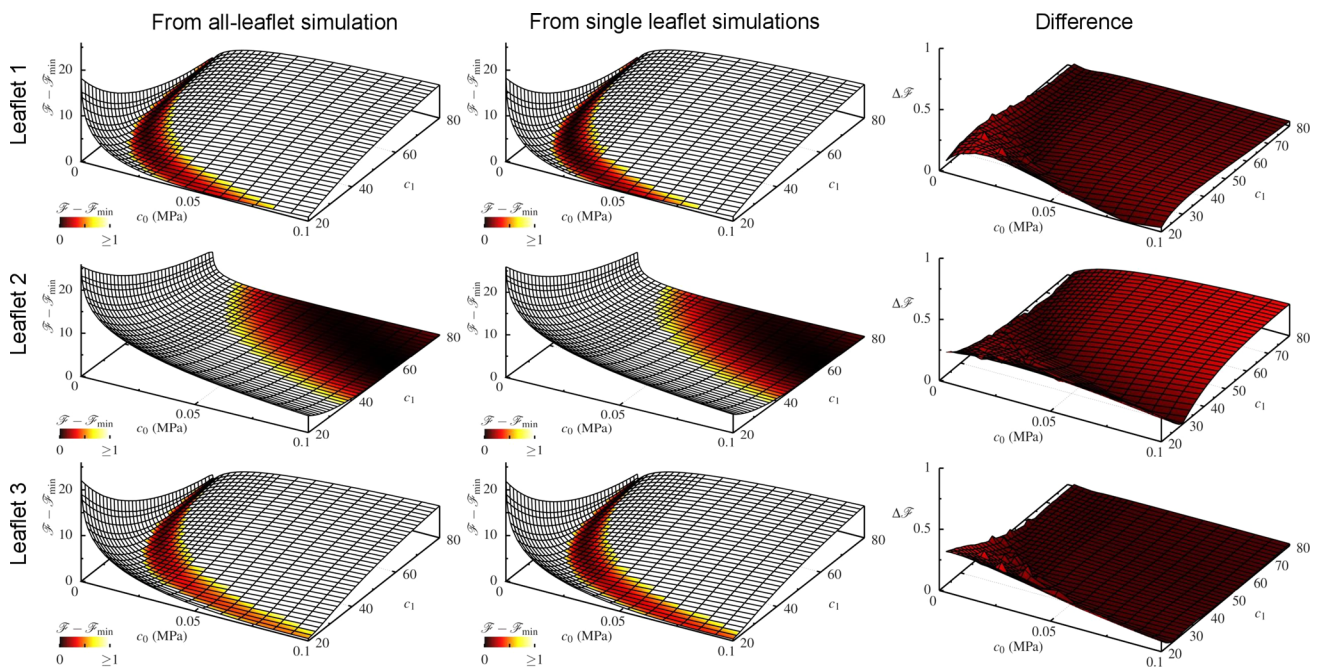


Fig. 8 Cost function for each leaflet using full simulation (from left—*column 1*) and single-leaflet simulation (*column 2*). The minimal difference, shown in *column 3*, indicates weak coupling between three leaflets as far as the objective function is concerned

The close match between all-leaflet and single-leaflet simulation results might not hold true for non-symmetric cases, e.g., native bicuspid aortic valve. Nevertheless, results from single-leaflet-based inverse model would still be expected to provide an initial estimate for the correct parameter values.

3.5 Sensitivity to simulation parameters

For in vitro dataset, estimates of many of the simulation parameters—the matrix stiffness, the Poisson's ratio, and friction between leaflets—were available. However, for in vivo application, one must know the sensitivity of results to various inputs, so that the confidence in results can be established. In varying the Poisson's ratio, the change in value of the cost function for all values of c_0 and c_1 was observed to be minimal. Therefore, although a close to incompressibility behavior ($\nu = 0.5$) is usually expected for soft tissues, in the current framework a lower Poisson's ratio (e.g., $\nu = 0.35$) can be used to improve the computational stability without affecting the final results. Similarly, the cost function, and, therefore, the effective stress-strain response, was predominantly insensitive to the frictional coefficient between the leaflets. The surface plots for change in cost function for these cases look very similar to Fig. 9a (very close to zero everywhere) and, thus, are skipped for brevity. In the case of varying matrix stiffness, the cost function changes slightly in the low $c_0 - c_1$ region (lower left corner of contour plot). This is an expected result because the fiber part of the stiffness is very soft in the low $c_0 - c_1$ region, thus making the

matrix part significant. However, this variation in the cost function does not alter the effective stress-strain response significantly. The size of this region in $c_0 - c_1$ parameter space, where the cost function is affected by the matrix stiffness, also depends on the thickness of the leaflets, such that the effect would be even smaller for thinner leaflets.

3.6 Effect of variation in fiber architecture

Numerous previous studies have demonstrated the importance of collagen fiber structure in the functionality of soft tissues, in general, and heart valve leaflets, in specific. The effective stress-strain response does not change significantly if the element-wise fiber splay (σ) is replaced by its average value assigned as a constant for all three leaflets (Fig. 9a). However, if the chosen constant value is different from the average value, the cost function changes slightly and non-homogeneously (Fig. 9b and c) indicating the sensitivity of our framework to the fiber structure. It is important to note that although the cost function itself changes with variation in fiber splay, the difference in the effective stress-strain response is extremely small, which is visualized by plotting the “iso-stress-strain minima” curve (numerically computed for these cases, since absolute minima in this case is unknown). Therefore, although not knowing the fiber splay precisely does not affect the results of the inverse model, current framework could, in principle, be used to detect changes in the fiber structure if it is treated as a degree of freedom in the optimization process. In other words, for correct estimates

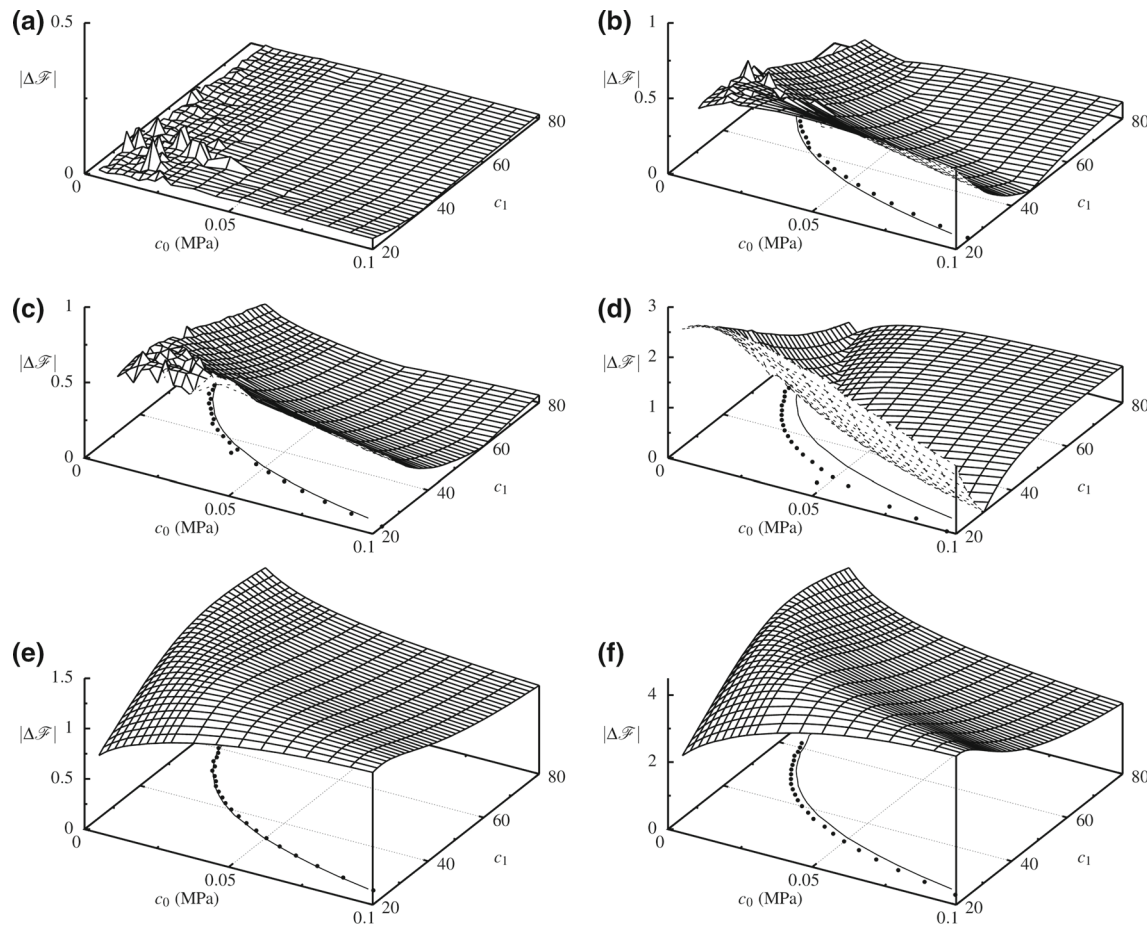


Fig. 9 (a–d) Changes in cost function (w.r.t. the base case) due to variation in fiber structure—**a** constant splay of 0.58 radians (average), **b** constant splay of 0.5 radians, and **c** constant splay of 0.8 radians, and **d** a generic circumferential direction assigned for the all the fibers. **e–f** Changes in the cost function due to noise in the input point cloud data

(w.r.t. the base case)—random Gaussian noise with standard deviation of 0.2 mm (**e**) and uniform/systematic noise (**f**). On the $c_0 - c_1$ plane, the line corresponds to the minima for base case and points correspond to that of the current case, indicating the shift in minima of the cost function

our inverse modeling approach requires only an approximation of the fiber splay and could be used to determine abnormal microstructure.

To determine the effect of fiber direction θ_0 on inverse modeling results, the leaflet-specific fiber directions are replaced by a generic circumferential fiber direction. In this case, the change in cost function is most pronounced (Fig. 9d), where the minima and effective stress-strain response also shift appreciably. This indicates that it is important to have accurate information about the direction of fibers in leaflets for correct final results. For native aortic valve leaflets the average fiber directions have been determined recently and were found to be consistent across population (Aggarwal et al. 2014). It should be noted that the spikes seen on the surface plots of difference in the cost function (Fig. 9) pertain to the numerical convergence issues: simulations at some parameter values fail to converge (purely due to numerical issues) and the results at

those points are interpolated from neighboring points in the parameter space. Therefore, the spikes in the difference plots are largely due to the corresponding interpolation error.

3.7 Effect of imaging resolution

Resolution of the imaging modality is a dominant factor in the application of current inverse modeling approach. The cost function varies slightly when a random noise is added to the point cloud data (Fig. 9e), and the change in the iso-stress-strain minima (i.e., effective stress-strain response) is negligible. However, the variation becomes much more distinct if a systematic (or a constant) error is introduced into the point cloud data (Fig. 9f). In the case of systematic error, the minima of the cost function also moves noticeably, altering the stress-strain response appreciably. This indicates the importance of high-resolution

imaging in the successful implementation of current framework, which was true for in vitro experimental setup. Since the only primary input to our framework is the shape of the leaflet, such a close relationship between resolution of imaging and the final results is not a surprising result.

3.8 Minimization and final fit errors

First, we start with the case when same set of c_0 and c_1 are assigned to all three leaflets. The minimization sequences for this case with different starting positions superimposed on a contour plot of the cost function are shown (Fig. 10). The iterations quickly converge to the iso-stress-strain minima region of the cost function. As the stress–strain curves in this region are almost identical, these results are considered

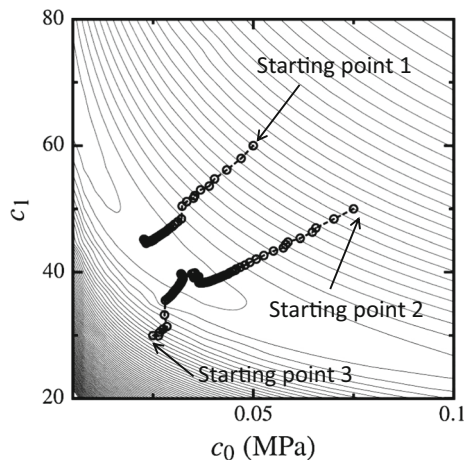


Fig. 10 Cost function for the base case using all frames plotted as a contour, with three minimization sequences shown with different starting points; all three sequences converge to the minima region of the contour indicating uniqueness of the solution

converged. Next, for the case when three leaflets are allowed to have different values of c_0 and c_1 , we first minimize using single-leaflet simulations to obtain a better initial guess and then use those estimates as a starting point for the full simulation. This substantially improves the computational speed. The resulting fit to the point cloud in this case is better than the first one where leaflets were constrained to have same c_0/c_1 values. The input point cloud with the absolute projection error and final fit of the deformed valve shape at the converged set of parameters is shown (Fig. 11), and the statistics of the minimized projection error are provided in Table 4. The average of the signed projection distance is very close to zero indicating that the final error is randomly distributed over the leaflet. The standard deviation in the absolute projection distance is less than 0.35 mm for all cases and the maximum absolute error is about 1.1 mm (which can be observed on leaflet 2, Fig. 11). Thus, the final surface fit obtained using our framework is excellent. Stress–strain relationship encountered during valve closing at a representative element in the center of leaflets using converged material parameters is shown in Fig. 12a. This demonstrates the predictive capabilities of current framework, as for obtaining this result the only input data used was 1) shape of the valve as it is loaded and 2) leaflets’ fiber structural information.

3.9 Validation against experimental results

For validation, the strain energy density calculated using the biaxial setup simulation at the biomechanical parameters obtained from the inverse model is plotted along with the experimental results (Fig. 12b). The responses are close but don’t match perfectly, especially for leaflet 2—which also showed higher error in the final fit (Fig. 11 and Table 4). Possible reasons for this discrepancy and the overall

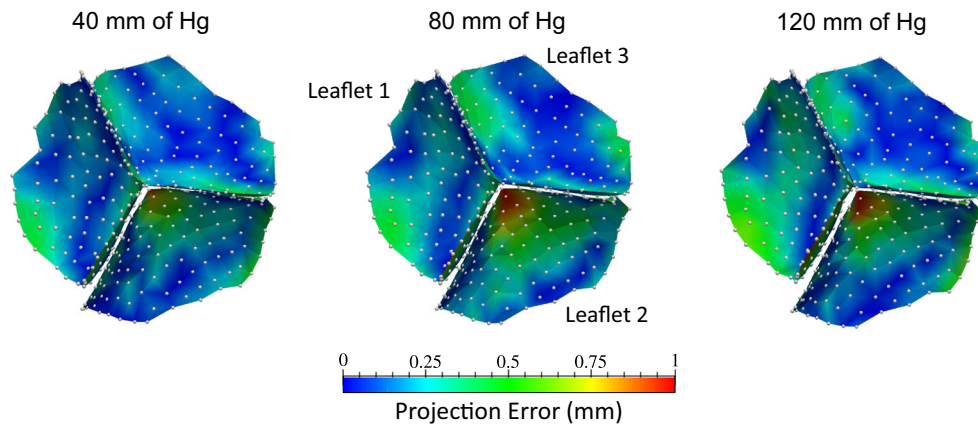


Fig. 11 Valve deformed shape and the input point cloud from experiment at three different pressures—40, 80 and 120 mm of Hg. The errors are minimal for all three leaflets, but are slightly higher for leaflet 2

Table 4 Statistics of the final fit to point cloud by evaluating mean, standard deviation and maximum of signed and unsigned projection distance

Pressure (mm)	Leaflet	Mean (d)	Mean (ldl)	Std (d)	Std (ldl)	Max (ldl)
40	1	-0.081	0.195	0.232	0.15	0.718
	2	0.008	0.238	0.31	0.196	0.977
	3	0.002	0.182	0.220	0.124	0.619
80	1	-0.125	0.214	0.242	0.169	0.786
	2	0.135	0.294	0.350	0.232	1.15
	3	-0.094	0.199	0.224	0.140	0.574
120	1	-0.214	0.270	0.272	0.216	0.938
	2	0.05	0.270	0.357	0.238	1.155
	3	-0.018	0.196	0.238	0.137	0.611

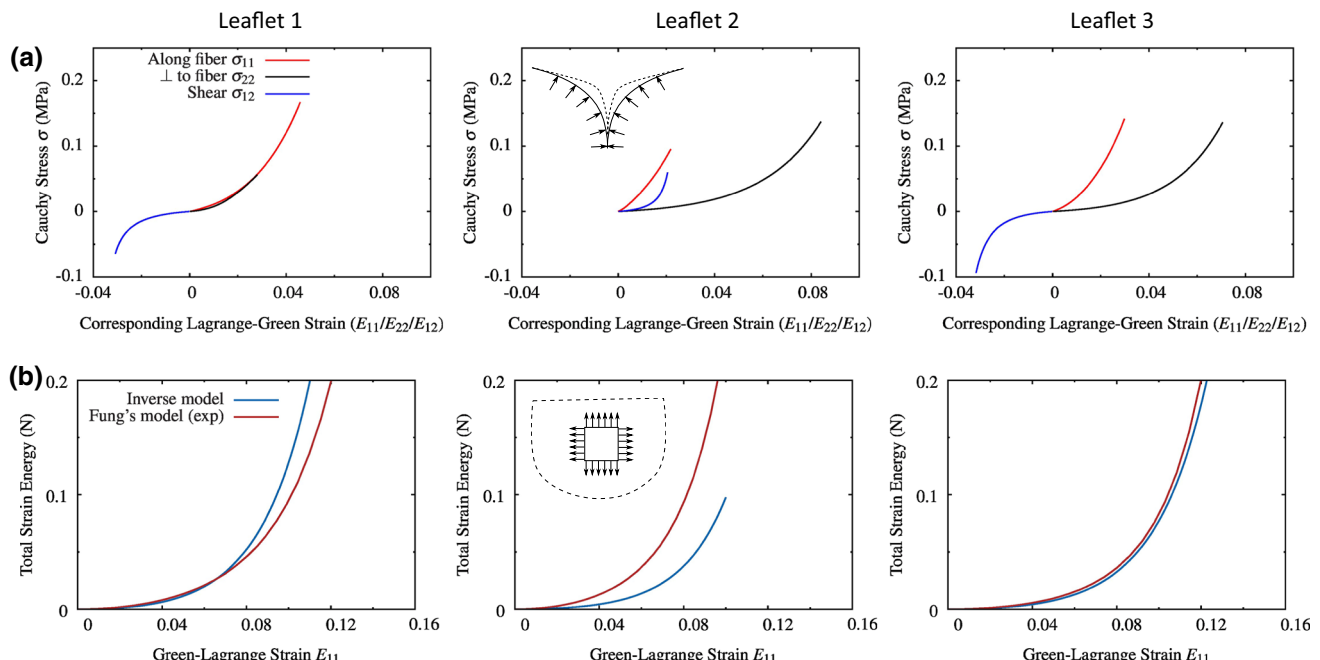


Fig. 12 **a** Stress–strain relation at the center of three leaflets during valve closing determined solely through current inverse modeling approach with the only input being imaging of leaflet as it is loaded. **b** Strain energy during equi-biaxial stress experiment compared with

the simulation (solid lines are using parameters obtained from inverse model and the points are from Fung's law coefficient obtained through biaxial experiment). The results match reasonably well

importance of results presented in this section are discussed next.

4 Discussion

4.1 Contributions of the present work

Biomechanical properties of heart valve leaflets play a critical role in determining their physiological function as well as susceptibility to disease. Abnormal mechanical leaflet behavior has been hypothesized to lead to changes in the stress state of VICs and, eventually, causing them to adopt a pathological phenotype (Poggio et al. 2013; Yip and Simmons 2011). Therefore, changes in the mechanical properties of

valve leaflets during their lifetime could be used as an indicator for pathological functionality. The current study presents an important step toward realizing a clinical tool that can be used to evaluate mechanical properties of heart valves from *in vivo* imaging without the need for excision.

Our focus was on development of a framework and determination of its feasibility, accuracy, and sensitivity to various properties of the valve, while exploiting known quantified tissue structures. This approach is non-conventional and a new direction in heart valve mechanics. Full development of such a technique that can be applied to *in vivo* human dataset involves many big challenges (Sect. 1). Therefore, in this work we focused on formulating and validating our framework in the context of *in vitro* dataset. This allowed us to carry out systematic sensitivity studies and establish a strong

confidence in the approach, while at the same time identify the areas where further work would be needed. In particular, we show that following the presented approach, we were able to accurately estimate the complete leaflet response to quasi-static loading with *most* two parameters per leaflet. Our framework produced very good agreement, and our results match reasonably well with the experimental data.

The results obtained here provide a critical insight into many facets of such a technique. The change in cost function as the pressure values and number of frames are varied (Fig. 6), for the first time, presents a quantitative estimate of the information needed for obtaining results with high confidence. Higher pressures cause the strains over leaflet to be more heterogeneous, thus improving the parameters estimation. The increase in cost function's convexity with increase in the number of frames is an expected result, and indicates that obtaining more number of frames from *in vivo* imaging will help improve the accuracy of our inverse modeling framework. Similarly, the pressures at which the valve should be imaged can be chosen judiciously in light of the present results.

The present framework is focused on obtaining correct stress-strain responses during valve closure which determines the cellular phenotypical state. Although one might anticipate the problem of uniqueness in the final parameters, the cost function for each and every case was seen to be convex with a unique global minimum, i.e., a unique set of optimal mechanical parameters (Figs. 5, 6, 8, 10). This clearly demonstrates that following our approach, where the fiber architecture is prescribed via structural model, the final parameters needed to produce a given deformed valve shape are unique. But, interestingly, even though the global minima and solution are unique, the observation regarding the existence of an iso-stress-strain minima region is an important one (Fig. 7). This further strengthens the point that one should not compare the values of mechanical parameters. Instead, the effective stress-strain response provides a more robust indicator for comparison of different tissue stiffness.

An important prerequisite for the success of an inverse model is the uniqueness of the solution, which comes from the convexity of objective cost function. The convexity we observe in our results is largely attributed to our ability to incorporate fiber structure through our constitutive model. Although Fung-type elastic models can incorporate preferred fiber direction through material axes definition, it is not possible to incorporate the fiber distribution, splay or orientation index. Furthermore, with higher number of parameters in the Fung's model, the convexity of the cost function was observed to be lost, creating problems with the convergence of our algorithm and uniqueness of the solution. These observations are consistent with the literature. Our research group has previously shown that the Fung's model parameters need constraints for its strain energy function to satisfy convexity

(Sun et al. 2005), while the structural model has been shown to be always convex (Lanir 1994).

The low sensitivity of our framework to the friction coefficient, Poisson's ratio, and the matrix stiffness are important results. These signify that only an approximate estimate of these properties will give an accurate assessment of leaflets' mechanical properties. It also suggests that one could tweak these parameters to improve the stability and speed of present method without affecting the results. For example, while simulating the initial part of valve loading, the matrix stiffness plays an important role in providing numerical stability as the fiber stiffness is small in this low-stress region. Therefore, a small value of matrix stiffness may cause instability issues in the forward model leading to convergence problems. The results presented here indicate that it would be acceptable to use a slightly higher value of matrix stiffness for improving the stability without affecting the outcome of our approach.

The sensitivity of the framework to the fiber structure is in many ways the most important result. Since an average value of the fiber splay gives an almost identical cost function (Fig. 9a), it suggests that population-averaged structural information (e.g., (Aggarwal et al. 2014)) might be useable in an otherwise patient-specific model. Furthermore, deviating from this average value produces only a negligible change in the effective stress-strain response (Fig. 9b, c). This indicates that differences in the fiber splay do not significantly affect the results of our framework. However, the absolute value of cost function is altered under these variations in the splay, and, therefore, in principle, variations in fiber splay could be detected from inverse modeling. For example, one could decouple the mechanical parameters and the fiber splay in the optimization process by minimizing the cost function with respect to parameters followed by with respect to the fiber splay. This direction in our inverse model development will be explored in the future so that it can be combined with the fiber splay differences found in pathological valves (Aggarwal et al. 2014).

We found that, unlike fiber splay, the fiber directions are critically important in obtaining an accurate result (Fig. 9d). Although the fiber directions in prosthetic valves vary widely, collagen fibers in the native valve leaflets are aligned predominantly along the circumferential direction. Therefore, while applying current framework to the native heart valves, one would have a good *a priori* estimate of the fiber direction. The relation of present framework's output and the fiber architecture (direction and splay) will be crucial for applying this tool to diagnose abnormalities in the heart valve function. We have shown previously one important effect of these differences, where the statistically important difference in the fiber splay of tricuspid and bicuspid aortic valves was indicated to be related to the higher risk of calcification disease (Aggarwal et al. 2014). The results presented here suggest that using our framework such differences might be detected

to diagnose asymptomatic valve diseases, allowing treatment at an early stage.

The resolution and accuracy of the imaging vary the effective stress-strain response slightly (Fig. 9 e, f) and, thus, form an important component for the success of the current approach. This is an expected result as the only input our method needs is the valve shape at different loading points, and thus, a high certainty in the input point cloud will lead to higher confidence in the final results. The computational speedup obtained by simulating a single leaflet was significant and provided a good starting point for the full valve simulation. In the case of non-symmetric native valves, a full valve simulation would be required for accurate final results. However, simulating single leaflet and using that result as an initial guess for the full simulation would provide a substantial speedup in the algorithm. The robustness of resulting stress-strain behavior with respect to the starting iteration point shows that the framework has good convergence properties (Figs. 5b, 10). The verification (Fig. 5c) and validation (Fig. 12b) of our framework provides confidence in this generalized technique of estimating mechanical properties of valve leaflets from imaging. Also, the final surface fit obtained using the current framework shows very small residual errors (Fig. 11). Therefore, the current framework lays the basis for a tool that would eliminate the need for excising leaflets for biomechanical studies.

4.2 Limitations and future directions

4.2.1 Imaging and segmentation

While it might be desirable to use the 3DUS images directly, here we focus on taking advantage of the advances in automatic segmentation techniques and, therefore, use the segmented point cloud that defines valve shape as the input to our framework. In the current study, high-resolution *in vitro* imaging dataset was used. High-resolution imaging of the heart valves *in vivo* is an ongoing challenge, and our ability to capture multiple frames during valve closure will be an important factor in the success of this approach. The advances in the ultrasound technology (Hung et al. 2007) and automatic segmentation of the images from ultrasound (c.f. (Pouch et al. 2015)) during the last decade will be paramount to the successful implementation of our framework to clinical use.

4.2.2 Computational speed and stability of algorithm

To make the problem computationally tractable, the full structural model was simplified by approximating the ensemble response. This allows us to utilize the fiber structure, however, at the cost of losing some information such as coupling of different fiber families. This becomes even more

important for the case of native valves, where different layers interact in a complicated fashion. Therefore, an improved computational approach will be required so that the full structural model can be employed without increasing the solution time significantly. Finally, the assumption of homogenous material behaviors over a leaflet is a good starting point, but limits the fidelity of our models and the amount of information they can provide. It is known that native heart valves have a distinctly different mechanical behavior in the belly, commissure and coaptation zones (Billiar and Sacks 2000b). Therefore, it will be important to relax this homogeneity constraint in the current framework, which will also necessitate faster and scalable algorithms. Utilizing advanced computational techniques, such as adaptively setting the λ parameter in Levenberg–Marquardt algorithm (14), multi-grid methods (Hackbusch 1985) and adjoint-based methods (Haslinger and Mäkinen 2003), would help alleviate these problems.

Associated with the computational efficiency will also be a need for improvement in the stability of our forward model. Its failure to converge in some cases represents a hurdle in implementing it in a clinical setting. The nature of exponential function leads to similar stress-strain behavior even while using widely different values of material parameters. This is a fundamental issue in any exponential-type material laws, and, since most of the soft tissue constitutive laws use an exponential function in some form, using a different stress-strain model would not solve this issue. Rather, a solution at the algorithm stage might be more suitable and will be investigated in the future.

4.2.3 Comparison with biaxial mechanical experimental data.

Perhaps the most subtle effect we observed during the validation of the study was the deviations encountered between the predicted strain energy function and that calculated experimentally. We believe the discrepancy is predominantly due to the effects of preconditioning and related inelastic effects of removing and sectioning the leaflets from the intact valve. Preconditioning is a part of the standard biomechanical experiment protocols and was used for obtaining the current experimental results. However, this effect remains poorly understood and has been shown to produce substantially different strain paths in the same tissue specimens subjected to varying preconditioning histories (Sacks 2000a). We note that the leaflets were not preconditioned before loading the intact valve under static pressure and that the strain path employed during biaxial tests was sufficiently different. On the other hand, the form and the overall agreement were fairly good (Fig. 12b), as well as the final fit of the valve shape was excellent (Fig. 11). Interestingly, since this framework estimates the mechanical behavior of valve leaflets directly in their *native* state, it removes artifacts of explant and extrap-

olation of in vitro results to in vivo. It may, in fact, provide a better estimate to the actual in vivo valve behavior.

4.2.4 Extension to in vivo

The present study was meant to be only a first but significant step in the direction of developing an in vivo heart valve evaluation tool. In order to extend this framework to in vivo dataset, many additional details would need to be added. One substantial difference in our in vitro model and native heart valves is that the basal attachment of native valves moves with the aorta. Thus, extension of present method to native valves will require implementation of moving annulus through boundary conditions. Similarly, the pressure applied on the valve in vitro was known to a high accuracy, and was used as a loading condition in the inverse model. For in vivo setting, measuring the transvalvular pressure at the precise moments as the valve is imaged will be a challenge. Additionally, in the present case, the bioprosthetic valve was chemically fixed, thus providing us with a well-known reference state. However, for native valves, one needs to determine the pre-strains present in the leaflet, so that reference state can be appropriately adjusted. Getting an estimate of the leaflet thickness from the images will be important as well. Lastly, the in vitro setup using in the current study provided quasi-static conditions. However, in vivo, the valve opens and closes constantly, making the inertial effects important. Therefore, the forward model would have to be adjusted to take into account the dynamic behavior of the valve closure.

5 Conclusions

The aim of this study was to construct a framework for determining the biomechanical properties of heart valve leaflets using only in vivo obtainable data and population-averaged fibrous maps. A comprehensive in vitro bioprosthetic heart valve dataset was used to comprehensively evaluate the approach. We determined accuracy levels for tissue property estimation using a comprehensive in vitro dataset in which the leaflet geometry, along with the actual experienced strains, mechanical behavior, and fibrous structures are known to a high level of precision. We utilized a simplified structural model for the leaflet material behavior, which allowed us to reduce the number of parameters to be determined per leaflet to only two. Moreover, it provided a way to exploit the prior knowledge about the population-averaged leaflet microstructure that recently became available. This approach allowed us to dramatically reduce the computational time, and easily visualize the cost function and minimization process. We observed the uniqueness of final stress-strain response using our approach and determined that image resolution is an important component in the accu-

racy of the presented framework. Furthermore, we found that an average fiber splay provides the same results as an exact mapped structure. Therefore, we noted that to apply this approach to in vivo data, our ability to use average fiber structure across populations will be extremely important in making this method applicable to clinically obtainable data. Even though small variations in the fiber structure do not affect the resulting stress-strain response, they change the absolute value of the cost function. These results suggest that, by extending our framework, differences in fiber structure could be detected to diagnose asymptomatic valve diseases, allowing treatment at an early stage. Combined with other important in vivo information like the annulus movement and reference configuration of the valve, this framework will form the essential basis for an in vivo diagnostic tool.

Acknowledgments We gratefully acknowledge the help from Will Zhang with parameter estimation and analysis of biaxial data. This work was supported by the American Heart Association Southwest Affiliate Postdoctoral Fellowship 14POST18720037 to A.A. and National Institutes of Health research grant R01 HL108330 to M.S.S. The authors acknowledge the Texas Advanced Computing Center (TACC) at The University of Texas at Austin for providing HPC resources that have contributed to the research results reported within this paper. URL: <http://www.tacc.utexas.edu>.

Funding This study was funded by National Institutes of Health (Grant Number R01 HL108330) and American Heart Association (Grant Number 14POST18720037).

Compliance with ethical standards

Conflicts of interest The authors declare that they have no conflict of interest.

6 Appendix

Exponential function of the form $f(c_0, c_1, x) = c_0(e^{c_1 x} - 1)$, where $x \in \mathbb{R}^+$ is the independent variable, is very common in soft tissue mechanics to describe the stress-strain behavior so that its stiffness increases linearly with stress. Here $c_0 \in \mathbb{R}^+$ and $c_1 \in \mathbb{R}^+$ are the material parameters that determine the quantitative nature of this function or stress-strain relationship. However, many different pairs of (c_0, c_1) values can give quite similar responses. To analyze this aspect, we first construct a functional that calculates the difference between two exponential functions with different set of parameters:

$$\mathcal{F}(c_0, c_1, \bar{c}_0, \bar{c}_1, \epsilon) = \int_0^\epsilon [c_0(e^{c_1 x} - 1) - \bar{c}_0(e^{\bar{c}_1 x} - 1)]^2 dx. \quad (15)$$

$\epsilon \in \mathbb{R}^+$ is the upper strain limit for a given application. For given values of \bar{c}_0 and \bar{c}_1 , this functional obviously has one absolute global minima at $c_0 = \bar{c}_0$ and $c_1 = \bar{c}_1$ for all

values of ϵ . However, to find the curve in $c_0 - c_1$ parameter space along which the function $f(c_0, c_1, \epsilon)$ is “closest” to $f(\bar{c}_0, \bar{c}_1, \epsilon)$, we minimize the functional \mathcal{F} for a given c_1 , i.e.,

$$\begin{aligned} & \arg \min_{c_0 \in \mathbb{R}^+} \mathcal{F}(c_0, c_1, \bar{c}_0, \bar{c}_1, \epsilon) \\ &= \arg \min_{c_0 \in \mathbb{R}^+} \int_0^\epsilon \left[c_0(e^{c_1 x} - 1) - \bar{c}_0(e^{\bar{c}_1 x} - 1) \right]^2 dx \\ &= c_0^{\min}(c_1, \bar{c}_0, \bar{c}_1, \epsilon) \end{aligned} \quad (16)$$

One can obtain a closed-form solution under reasonable conditions (which are satisfied if $\epsilon \leq 1$, something usually true for strain):

$$\begin{aligned} c_0^{\min} [g(2c_1) - 2g(c_1) + 1] \\ = \bar{c}_0 [g(c_1 + \bar{c}_1) - g(c_1) - g(\bar{c}_1) + 1], \end{aligned} \quad (17)$$

where,

$$g(c_1) = \frac{e^{c_1 \epsilon} - 1}{c_1 \epsilon}. \quad (18)$$

References

- Abelev B et al (2013) Directed flow of charged particles at midrapidity relative to the spectator plane in Pb-Pb collisions at radical(s(NN))=2.76 TeV. *Phys Rev Lett* 111:232302
- Aggarwal A, Aguilar VS, Lee C-H, Ferrari G, Gorman JH, Gorman RC, Sacks MS (2013) Patient-specific modeling of heart valves: from image to simulation. In: Functional imaging and modeling of the heart. Springer, pp 141–149. doi:[10.1007/978-3-642-38899-6_17](https://doi.org/10.1007/978-3-642-38899-6_17)
- Aggarwal A et al (2014) Architectural trends in the human normal and bicuspid aortic valve leaflet and its relevance to valve disease. *Ann Biomed Eng* 42:986–998. doi:[10.1007/s10439-014-0973-0](https://doi.org/10.1007/s10439-014-0973-0)
- Amini R et al (2012) On the in vivo deformation of the mitral valve anterior leaflet: effects of annular geometry and referential configuration. *Ann Biomed Eng* 40:1455–1467. doi:[10.1007/s10439-012-0524-5](https://doi.org/10.1007/s10439-012-0524-5)
- Besl PJ, Mckay ND (1992) A method for registration of 3-D shapes. *Ieee T Pattern Anal* 14:239–256. doi:[10.1109/34.121791](https://doi.org/10.1109/34.121791)
- Betsch P, Gruttmann E, Stein E (1996) A 4-node finite shell element for the implementation of general hyperelastic 3D-elasticity at finite strains. *Comput Methods Appl Mech Eng* 130:57–79
- Billiar KL, Sacks MS (2000a) Biaxial mechanical properties of the native and glutaraldehyde-treated aortic valve cusp: Part II-A structural constitutive model. *J Biomech Eng* 122:327–335
- Billiar KL, Sacks MS (2000b) Biaxial mechanical properties of the natural and glutaraldehyde treated aortic valve cusp-Part I: Experimental results. *J Biomech Eng* 122:23–30
- Christie GW, Barratt-Boyes BG (1995) Mechanical properties of porcine pulmonary valve leaflets: how do they differ from aortic leaflets? *Ann Thorac Surg* 60:S195–199
- Cortes DH, Lake SP, Kadlowec JA, Soslowsky LJ, Elliott DM (2010) Characterizing the mechanical contribution of fiber angular distribution in connective tissue: comparison of two modeling approaches. *Biomech Model Mechanobiol* 9:651–658. doi:[10.1007/s10237-010-0194-x](https://doi.org/10.1007/s10237-010-0194-x)
- Einstein DR, Freed AD, Stander N, Fata B, Vesely I (2005) Inverse parameter fitting of biological tissues: a response surface approach. *Ann Biomed Eng* 33:1819–1830. doi:[10.1007/s10439-005-8338-3](https://doi.org/10.1007/s10439-005-8338-3)
- Fan R, Sacks MS (2014) Simulation of planar soft tissues using a structural constitutive model: finite element implementation and validation. *J Biomech* 47:2043–2054
- Fung YC (1993) Biomechanics: mechanical properties of living tissues, 2nd edn. Springer Verlag, New York
- Gloeckner DC, Billiar KL, Sacks MS (1999) Effects of mechanical fatigue on the bending properties of the porcine bioprosthetic heart valve. *Asaio J* 45:59–63
- Hackbusch W (1985) Multi-grid methods and applications. Springer series in computational mathematics, vol 4. Springer-Verlag, Berlin; New York
- Haslinger J, Mäkinen RAE (2003) Introduction to shape optimization: theory, approximation, and computation: advances in design and control. SIAM, Society for Industrial and Applied Mathematics, Philadelphia
- Hughes TJR, Liu WK (1981a) Non-linear finite-element analysis of shells-part 1: three-dimensional shells. *Comput Method Appl M* 26:331–362. doi:[10.1016/0045-7825\(81\)90121-3](https://doi.org/10.1016/0045-7825(81)90121-3)
- Hughes TJR, Liu WK (1981b) Non-linear finite-element analysis of shells- part 2: two-dimensional shells. *Comput Method Appl M* 27:167–181. doi:[10.1016/0045-7825\(81\)90148-1](https://doi.org/10.1016/0045-7825(81)90148-1)
- Hung J et al (2007) 3D echocardiography: a review of the current status and future directions. *J Am Soc Echocardiogr* 20:213–233. doi:[10.1016/j.echo.2007.01.010](https://doi.org/10.1016/j.echo.2007.01.010)
- Kamensky D et al (2015) An immersogeometric variational framework for fluid-structure interaction: application to bioprosthetic heart valves. *Comput Methods Appl Mech Eng* 284:1005–1053. doi:[10.1016/j.cma.2014.10.040](https://doi.org/10.1016/j.cma.2014.10.040)
- Krishnamurthy G et al (2008) Material properties of the ovine mitral valve anterior leaflet in vivo from inverse finite element analysis. *Am J Physiol Heart Circ Physiol* 295:H1141–H1149. doi:[10.1152/ajpheart.00284.2008](https://doi.org/10.1152/ajpheart.00284.2008)
- Lanir Y (1994) Plausibility of structural constitutive-equations for isotropic soft-tissues in finite static deformations. *J Appl Mech-T Asme* 61:695–702
- Lee CH, Amini R, Gorman RC, Gorman JH 3rd, Sacks MS (2014) An inverse modeling approach for stress estimation in mitral valve anterior leaflet valvuloplasty for in-vivo valvular biomaterial assessment. *J Biomech* 47:2055–2063. doi:[10.1016/j.jbiomech.2013.10.058](https://doi.org/10.1016/j.jbiomech.2013.10.058)
- Lee CH, Carruthers CA, Ayoub S, Gorman RC, Gorman JH 3rd, Sacks MS (2015) Quantification and simulation of layer-specific mitral valve interstitial cells deformation under physiological loading. *J Theor Biol* 373:26–39. doi:[10.1016/j.jtbi.2015.03.004](https://doi.org/10.1016/j.jtbi.2015.03.004)
- Liu DC, Nocedal J (1989) On the limited memory bfgs method for large-scale optimization. *Math Progr* 45:503–528. doi:[10.1007/Bf01589116](https://doi.org/10.1007/Bf01589116)
- Maas SA, Ellis BJ, Ateshian GA, Weiss JA (2012) FEBio: finite elements for biomechanics. *J Biomed Eng* 134:011005. doi:[10.1115/1.4005694](https://doi.org/10.1115/1.4005694)
- Mirnajafi A, Raymer J, Scott MJ, Sacks MS (2005) The effects of collagen fiber orientation on the flexural properties of pericardial heterograft biomaterials. *Biomaterials* 26:795–804
- Ophir J, Cespedes I, Ponnekanti H, Yazdi Y, Li X (1991) Elastography: a quantitative method for imaging the elasticity of biological tissues. *Ultrasonic imaging* 13:111–134
- Poggio P et al (2013) Noggin attenuates the osteogenic activation of human valve interstitial cells in aortic valve sclerosis. *Cardiovasc Res* 98:402–410. doi:[10.1093/cvr/cvt055](https://doi.org/10.1093/cvr/cvt055)
- Pouch A et al. (2015) Segmentation of the Aortic valve apparatus in 3D echocardiographic images: deformable modeling of a branching medial structure. In: Camara O, Mansi T, Pop M, Rhode K,

- Sermesant M, Young A (eds) Statistical atlases and computational models of the heart - imaging and modelling challenges. Lecture notes in computer science. Springer International Publishing, pp 196–203. doi:[10.1007/978-3-319-14678-2_20](https://doi.org/10.1007/978-3-319-14678-2_20)
- Raghupathy R, Barocas VH (2009) A closed-form structural model of planar fibrous tissue mechanics. *J Biomech* 42:1424–1428. doi:[10.1016/j.jbiomech.2009.04.005](https://doi.org/10.1016/j.jbiomech.2009.04.005)
- Rajamannan NM (2013) Cardiac valvular medicine. Springer, Dordrecht
- Rausch MK, Famaey N, Shultz TO, Bothe W, Miller DC, Kuhl E (2013) Mechanics of the mitral valve: a critical review, an in vivo parameter identification, and the effect of prestrain. *Biomech Model Mechanobiol* 12:1053–1071. doi:[10.1007/s10237-012-0462-z](https://doi.org/10.1007/s10237-012-0462-z)
- Sacks M (2000a) Biaxial mechanical evaluation of planar biological materials. *J Elasticity* 61:199–246
- Sacks MS (1999) A method for planar biaxial mechanical testing that includes in-plane shear. *J Biomed Eng* 121:551–555
- Sacks MS (2000b) A structural constitutive model for chemically treated planar connective tissues under biaxial loading. *Comput Mechanics* 26:243–249
- Sacks MS (2000c) A structural constitutive model for chemically treated planar tissues under biaxial loading. *Comput Mechanics* 26:243–249. doi:[10.1007/S004660000175](https://doi.org/10.1007/S004660000175)
- Sacks MS (2003) Incorporation of experimentally-derived fiber orientation into a structural constitutive model for planar collagenous tissues. *J Biomed Eng* 125:280–287
- Sacks MS (2004) A structural model for the native pulmonary valve. In: Yacoub M (ed) advances in tissue engineering and biology of heart valves. Florence, SHVD
- Sacks MS, Chuong CJ (1998) Orthotropic mechanical properties of chemically treated bovine pericardium. *Ann Biomed Eng* 26:892–902
- Sacks MS, Merryman WD, Schmidt DE (2009) On the biomechanics of heart valve function. *J Biomech* 42:1804–1824. doi:[10.1016/j.jbiomech.2009.05.015](https://doi.org/10.1016/j.jbiomech.2009.05.015)
- Sacks MS, Smith DB, Hiester ED (1997) A small angle light scattering device for planar connective tissue microstructural analysis. *Ann Biomed Eng* 25:678–689
- Schenk O, Gartner K (2004) Solving unsymmetric sparse systems of linear equations with PARDISO. *Future Gener Comp Sy* 20:475–487. doi:[10.1016/j.future.2003.07.011](https://doi.org/10.1016/j.future.2003.07.011)
- Schroeder W, Martin K, Lorensen B (1998) The visualization toolkit, 2nd edn. Prentice Hall PTR, Upper Saddle River
- Stephens EH, de Jonge N, McNeill MP, Durst CA, Grande-Allen KJ (2010) Age-related changes in material behavior of porcine mitral and aortic valves and correlation to matrix composition. *Tissue Eng Part A* 16:867–878. doi:[10.1089/ten.tea.2009.0288](https://doi.org/10.1089/ten.tea.2009.0288)
- Sun W, Abad A, Sacks MS (2005) Simulated bioprosthetic heart valve deformation under quasi-static loading. *J Biomed Eng* 127:905–914
- Sun W, Sacks MS (2005) Finite element implementation of a generalized Fung-elastic constitutive model for planar soft tissues. *Biomech Model Mechanobiol* 4:190–199
- Veress AI, Gullberg GT, Weiss JA (2005) Measurement of strain in the left ventricle during diastole with cine-MRI and deformable image registration. *J Biomed Eng* 127:1195–1207
- Wrighers P, Laursen TA (2007) Computational contact mechanics. CISM courses and lectures. Springer, New York
- Yip CY, Simmons CA (2011) The aortic valve microenvironment and its role in calcific aortic valve disease. *Cardiovasc Pathol* 20:177–182. doi:[10.1016/j.carpath.2010.12.001](https://doi.org/10.1016/j.carpath.2010.12.001)